

FIRST PRINCIPLES INVESTIGATIONS OF
SOLID-SOLID INTERFACES IN LITHIUM BATTERY MATERIALS

BY

NICHOLAS LEPLEY

A Thesis Submitted to the Graduate Faculty of
WAKE FOREST UNIVERSITY GRADUATE SCHOOL OF ARTS AND
SCIENCES

in Partial Fulfillment of the Requirements

for the Degree of

DOCTOR OF PHILOSOPHY

Physics

December 2015

Winston-Salem, North Carolina

Approved By:

Natalie Holzwarth, Ph.D., Advisor

Akbar Salam, Ph.D., Chair

William Kerr, Ph.D.

Freddie Salsbury Jr., Ph.D.

Timo Thonhauser, Ph.D.

Table of Contents

I	Context	1
	Chapter 1 Battery Overview	2
1.1	Long term: a global perspective	2
1.2	Medium term: battery functional properties	3
1.2.1	Energy density	4
1.2.2	Power density	5
1.2.3	Stability and lifetime	6
1.3	Near term: state of the art Li-ion batteries	7
1.4	Near term: promising research directions	9
	Chapter 2 Computational Theory	12
2.1	Quantum mechanics	12
2.2	Born-Oppenheimer approximation	13
2.3	Hohenberg-Kohn theorem	14
2.4	Independent electron approximation	16
	Chapter 3 Interfaces Between Crystalline Materials	18
3.1	Conceptual overview	18
3.2	Interface formalism	19
II	Novel Results	22
	Chapter 4 Methods	23
4.1	Basic	23
4.2	Interface representations	24
	Chapter 5 Li₂O/Li System	26
5.1	Li ₂ O/Li interfaces	26
5.2	Interface partial density of states	27
	Chapter 6 Li₂S/Li System	31
6.1	Li ₂ S/Li interfaces	31
6.2	Interface partial density of states	34

Chapter 7	Li₃PO₄/Li System	36
7.1	Li ₃ PO ₄ /Li interfaces	37
7.2	Interface partial density of states	38
Chapter 8	Li₃PS₄ Interfaces	40
8.1	Li ₃ PS ₄ /Li	42
8.2	Li ₃ PS ₄ /Li partial density of states	42
8.3	Li ₃ PS ₄ /Li ₂ S	43
8.4	Li ₃ PS ₄ /Li ₂ S partial density of states	44
Chapter 9	Summary and Conclusions	46
9.1	Interface energy summary	46
9.2	Interface reactions	48
9.3	Conclusions	53
III	Curriculum Vitae	61

List of Figures

1.1	Charge/discharge curves for two different electrodes	5
1.2	Schematic of Li-ion battery	8
5.1	Li ₂ O bulk structure	27
5.2	Structures of Li ₂ O interfaces	28
5.3	Interface energies for Li ₂ O interfaces	29
5.4	Li ₂ O interface density of states	30
6.1	Li ₂ S bulk structure	32
6.2	Li ₂ S interface structures	33
6.3	Li ₂ S interface energies	34
6.4	Density of states for Li ₂ S and Li metal	35
6.5	Li ₂ S interface density of states	35
7.1	Li ₃ PO ₄ interface structures	37
7.2	Li ₃ PO ₄ interface energies	38
7.3	Li ₃ PO ₄ interface density of states	39
8.1	Structure of Li ₃ PS ₄ /Li interface	41
8.2	Li ₃ PS ₄ /Li interface energy	41
8.3	Li ₃ PS ₄ interface density of state	43
8.4	Li ₃ PS ₄ /Li ₂ S interface structure	44
8.5	Li ₃ PS ₄ /Li ₂ S interface energy	45
8.6	Li ₃ PS ₄ /Li ₂ S interface density of states	45
9.1	Li ₃ PO ₄ /Li interface with Li defect	49
9.2	Density of states for Li ₃ PO ₄ /Li interface with a defect	51
9.3	Energy needed to move an oxygen away from Li ₃ PO ₄ at interface	52

List of Tables

5.1	Li ₂ O Data Table	26
7.1	Li ₃ PO ₄ Data Table	36
8.1	Li ₃ PS ₄ Data Table	40
9.1	Interface energetics summary	47

List of Abbreviations

DFT	Density Functional Theory
GGA	Generalized Gradient Approximation
HOMO	Highest Occupied Molecular Orbital
LDA	Local Density Approximation
LUMO	Lowest Unoccupied Molecular Orbital
SEI	Solid Electrolyte Interphase

Abstract

This work explains some of the current issues driving the development of Li batteries and some of the current research opportunities. In particular it focuses on using ab initio theoretical methods to model electrode/electrolyte interfaces for inorganic solid electrolyte materials, especially those related to Li_3PS_4 . I develop a general scheme based on the interface energy for analyzing interfaces between crystalline solids, quantitatively including the effects of varying configurations and lattice strain. This scheme is successfully applied to the modeling of likely interface geometries of several solid state battery materials including Li metal, Li_3PO_4 , Li_3PS_4 , Li_2O , and Li_2S . This formalism, together with partial density of states analysis, allows me to characterize the extent, stability, and transport properties of these interfaces. My investigation finds that all of the interfaces in this study are stable with the exception of $\text{Li}_3\text{PS}_4/\text{Li}$. For this chemically unstable interface, the partial density of states helps to identify mechanisms associated with the interface reactions. The energetic measure of interfaces and analysis of the band alignment between interface materials indicate multiple factors which may be predictors of interface stability, an important property of electrolyte systems.

Author's Note

The novel results in this work are primarily focused on simulations of solid-solid interfaces between Li metal and various Li solid electrolytes. The results themselves are, by and large, comprehensible without the context presented in the early chapters. It is comparatively easy to describe a set of results and how they were arrived at, but far more difficult to elucidate why those results were sought instead of others. The question of why is much larger than the questions of what and how, and answering it requires information only loosely related to the specific results. Nonetheless, the decisions of what systems to study and how best to investigate them are scientific questions that demand to be answered with evidence and argument no less careful than that applied to analyzing the results of such a study, and it is to these larger questions that I first direct your attention.

Part I
Context

Chapter 1

Battery Overview

1.1 Long term: a global perspective

Human civilization, like all complex ordered systems, must transport energy to each of its various parts and subsystems. While energy can exist in myriad forms, the energy flows within the world economy are overwhelmingly either chemical or electrical in nature. Chemical energy plays such a prominent role because it is not extraordinarily difficult to store, access, or transport. Similarly, electrical energy, although somewhat more difficult to store, can be quickly transported along power lines and can be readily converted into other forms of energy.

A rechargeable battery is an energy storage device and transducer that converts chemical energy to electrical energy and vice versa. It combines some of the versatility of electrical energy with chemical energy's portability and ability to be stored. The interest in an energy carrier with this combination of properties has increased dramatically in recent years due to several factors.

One of these factors is a desire to move away from the current dominant form of chemical energy usage, the burning of hydrocarbon fossil fuels. Fossil fuels represent the primary form of global energy distribution due to their ease of storage, access, and transport, but they lack a similarly reliable means of production. The primary downside of fossil fuels is thus that fossil fuel usage is not reversible. The combustion of fossil fuels releases carbon dioxide into the atmosphere which cannot easily be recaptured and turned back into fossil fuels. The release of carbon associated with the large-scale burning of fossil fuel for energy alters the chemical composition of the atmosphere, resulting in difficult to predict changes in climate and environment. Equally problematic, easily obtainable fossil fuels are a somewhat limited resource. This not only leads to concerns about their long term availability, but has also contributed to several supply shocks undesirable in such a crucial element of the world economy.

Considerable progress has been made in harvesting energy from renewable energy sources such as solar and wind power, typically transforming light and mechanical energy respectively into electrical energy. The intermittent nature of renewable energy sources necessitates storing that energy in some form, and storing that energy

chemically using rechargeable batteries is among the most versatile solutions. Battery technology is thus viewed as a key enabler of renewable energy generation.

The flexibility of electrical energy has enabled the creation of electronic devices, sophisticated mechanisms that use electrical energy to produce precisely patterned light and sound and to process information. The cost and size of these devices has decreased to such an extent that one of the major factors limiting their deployment is the challenge of supplying them with the electrical energy that they need to operate. Batteries are currently the only serious solution for this problem, and battery technology is thus a necessity for advanced portable electronics.

However energy is produced and consumed, it will almost certainly be stored chemically for the foreseeable future. Batteries allow this chemical energy to be moved via existing electrical energy distribution infrastructure and to leverage the ease with which electrical energy can be converted into light, sound, mechanical energy, etc. Equivalently, batteries enable the long term storage of electrical energy as well as the transport of that energy separate from the electric grid.

While the current size of and growth rate of the lithium ion battery market, circa 13 billion dollars with 12% growth per annum, may be sufficient motivation for studying battery technology, the underlying physical justifications indicate the fundamental nature of the problems batteries are being used to address.

1.2 Medium term: battery functional properties

In order to discuss the ways in which batteries can be improved, it is first necessary to understand what set of properties a rechargeable battery should exhibit. A detailed understanding of the properties of an ideal battery can be readily translated into the properties of individual materials, and determining materials properties is the focal point of this work. While the relative importance of the various attributes will depend on the specific application, the general characteristics of an ideal battery are relevant over a wide range of use cases.

In approximate order of importance: an ideal rechargeable battery stores a large amount of electrochemical energy in a small mass and volume. It is capable of being rapidly charged and discharged without altering its structure. The battery operates over a wide range of temperatures and pressures, especially those typical of the Earth's surface. The battery's properties are relatively unchanged by the passage of time, the number of charge/discharge cycles, and the extent of discharge. The battery remains shelf stable regardless of state of charge and exhibits limited self-discharge. Additionally, the ideal battery is made of inexpensive, inherently safe materials that are unlikely to burn, poison, or otherwise harm people who come into contact with them during either the normal operation of the battery or in any of its likely failure conditions. While some of these criteria, such as safety, require little explanation, most of them require further explication before they can be readily translated into the properties of individual materials.

1.2.1 Energy density

The electrical energy E stored in a battery can be written as the product of the mobile charge Q and the battery voltage ΔV , giving the relation $E = Q\Delta V$. Alternatively, the energy can be expressed as the product of the number of mobile ions/associated electrons N and the difference in the chemical potential experienced by those electrons at the two electrodes $\Delta\mu$, yielding the equivalent expression $E = \Delta\mu N$. Dividing either expression by the battery mass gives an expression for the energy density of a battery. In order to increase the energy density of a battery it is necessary to either increase the charge carrier density or to increase the voltage/chemical potential difference between the two electrodes.

The theoretical charge density, or theoretical capacity, of an electrode material can be determined by dividing the mobile ion charge per formula unit by the per formula unit mass. For battery applications this charge density is typically expressed in units of mAh/g. Metallic Li, for example, has a theoretical capacity of 3861 mAh/g, equivalent to the fundamental charge divided by the atomic mass of Li. As a point of comparison, a graphite anode with the chemical formula LiC_6 when fully charged has a capacity of 372 mAh/g. The theoretical capacity is theoretical because it assumes that all of the Li atoms in the electrode are mobile charge carriers in the battery, which may not be a valid assumption for all materials. In addition to the electrode capacities, the total energy density will also depend on the weight of the electrolyte and the other battery components.

One mechanism for increasing the theoretical capacity of an electrode material is to have divalent cations such as Mg instead of monovalent ones like Li as the charge carrying ions in the battery. While the specific capacity of pure magnesium is 2190 mAh/g, significantly less than the 3861 mAh/g value associated with metallic Li, this is due to the exceptionally low atomic weight of lithium metal. For cathode materials and other non-elemental electrodes the mobile ion often represents a relatively insignificant fraction of the total electrode weight. In those cases, the additional charge per ion can dramatically increase and even double the theoretical capacity.

The downside of the divalent ion approach is that the different charge states associated with divalent ions create variation in the chemical environment around those ions. In other words, the energy needed to oxidize Mg is different from that needed to further oxidize Mg^{+1} . Because the battery voltage is proportional to the chemical potential difference between the electrodes, the voltage difference between the terminals of a battery with divalent charge carriers will vary strongly and non-linearly as a function of charge state. This difficulty is illustrated in figure 1.1, which shows a comparison of the behavior of the voltage as a function of charge state for both a Mg electrode and a Li-ion electrode. The variation in the voltage profile as a function of charge state is a significant engineering problem that will have to be resolved in order for batteries based on divalent charge carriers to be practical.

While this problem is unavoidable for electrodes containing divalent charge carriers, variation in the ion chemical environment as a function of state of discharge is common in many potential electrode materials. Electrodes with different types of Li sites, such as $\text{Li}_2\text{Mn}_2\text{O}_4$, which has both tetrahedral and octahedral Li sublat-

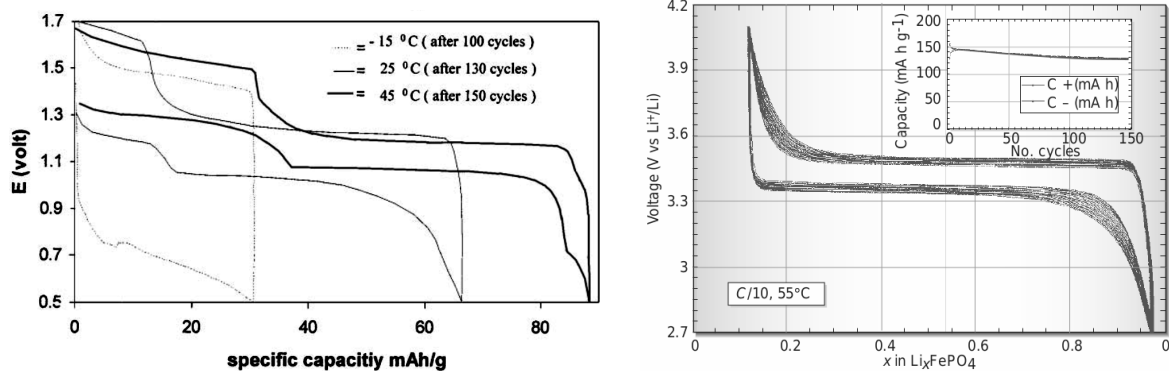


Figure 1.1: Charge and discharge curves showing Voltage as a function of charge state for both a Mg-ion electrode based on $Mg_x Mo_3 S_4$ (left) and a Li-ion electrode based on $LiFePO_4$ (right). The Mg-ion electrode exhibits a two-tiered discharge profile consistent with magnesium’s two valence electrons, while the discharge profile for the Li-ion electrode is much flatter. Figures adapted from references 1 and 2 with permission from Elsevier and Nature Publishing Group.

tices, may have strongly two-tiered voltages caused by the energy difference between the different Li sites. This highlights part of the difficulty in battery material design, where high performance for one desired property often comes at the expense of another desired property.

In addition to the electrode charge density, the energy of the battery depends on the voltage difference between the two electrodes. This voltage difference arises due to a difference in the electron chemical potential (i.e. the Fermi level) between the electrode materials. These potential differences, have been experimentally determined for many materials and are often expressed as voltages relative to a standard hydrogen electrode. Metallic Li makes an excellent battery material from a voltage standpoint because it has a voltage of -3.04 volts relative to the standard hydrogen electrodes; of the elements reported in the CRC Handbook of Chemistry and Physics, only Sr and Ca have lower electrochemical voltages.³ While the standard voltages are defined in terms of the neutral hydrogen electrode, for convenience the voltages given in the remainder of this work are expressed relative to Li metal unless otherwise specified.

Likely electrode materials are thus selected primarily on the basis of their theoretical capacity and relative voltage, with a flat discharge curve being another desirable property.

1.2.2 Power density

It is not enough for a battery to be capable of storing large quantities of energy. To be useful, the battery must also be capable of taking in and releasing that energy rapidly. The limiting factor in the charging and discharging of the battery is typically the rate at which ions move through the battery. The electrical power (P) in a circuit is given by the product of the circuit voltage (V) and the current (I) according to

the relation $P = IV$. Charge neutrality dictates that the charge flow carried by the electrons moving through an external circuit cannot exceed the flow rate of the ions within the battery. An ideal battery thus contains two electrodes which are capable of rapidly transporting both ions and electrons, and an electrolyte that has efficient ionic transport while remaining electrically insulating.

While ideal battery electrodes would allow rapid ionic diffusion, in practice the ionic conduction in the electrodes is often too slow for power battery applications. The typical geometry of a power battery cell has small particles of the electrode material connected by a loose network of liquid electrolyte and carbon black. This dramatically increases the surface area of the electrode, and greatly diminishes the distance that any given Li needs to migrate within the electrode material.

Rapid charging or discharging of a battery subjects it to non-equilibrium thermodynamic forces, and these forces may result in concentrations of ions and charge that differ strongly from the bulk values. These altered concentrations are particularly likely to occur at the interface between the electrode and electrolyte materials, since any difference in ionic conductivity between the two materials will tend to result in either a pile-up or a depletion at the interface. Battery interfaces thus need to function well not only at equilibrium, but at non-equilibrium concentrations that may occur as a result of charging or discharging the battery.

1.2.3 Stability and lifetime

In order to be practical, a rechargeable battery is expected to be capable of being charged and discharged hundreds or thousands of times over months or years of calendar time. In order to exhibit this degree of stability, the electrodes must have a crystal structure that is capable of accommodating additional ions without undergoing a dramatic change in shape or volume that would disrupt the crystal. The electrode materials must also not chemically react with the electrolyte, either at equilibrium or during battery charging and discharging.

This latter condition is difficult to fulfill in high power batteries because the electrolyte is simultaneously in contact with both the anode material, which has a high Fermi level and is a strong electron donor, as well as in contact with the cathode material, which is a strong electron acceptor. A stable crystalline electrolyte material must then have a wide band gap, or if the electrolyte is molecular, it must possess a wide separation between its highest occupied and lowest unoccupied molecular orbitals. Without this wide gap, the electrolyte will tend to be reduced by the anode material or oxidized by the cathode material or both.

Electrolyte materials are thus selected on the basis of their ionic conductivity for high power applications and on their ability to form electrochemically stable interfaces with both of the battery electrodes.

1.3 Near term: state of the art Li-ion batteries

In this section I detail the materials used in current Li-ion batteries, and evaluate to what extent their properties resemble those of an ideal rechargeable battery.

The term Li-ion battery typically refers to a cell which does not contain free Li metal, but which has layered electrode materials into which Li is inserted on both sides of the cell. The first commercially successful Li-ion battery was released in 1991 by the Sony corporation for use in mobile phones, and it combined a graphite anode with a LiCoO_2 cathode. This formulation remains one of the most popular Li-ion chemistries and a model version of it is shown in Figure 1.2. In the figure, the Li ions occupy the gaps between the 2D layers in both of the electrodes, a process known as intercalation. The small size of Li allows the transitions from $\text{LiCoO}_2 \leftrightarrow \text{Li}_{1-x}\text{CoO}_2$ and $\text{C} \leftrightarrow \text{Li}_y\text{C}_6$ to occur relatively reversibly and with a small enough volume change in the electrodes to avoid compromising the battery's integrity.

The intercalation electrode materials have much lower theoretical capacities than metallic Li. The theoretical capacity of LiC_6 is 372 mAh/g while for LiCoO_2 the theoretical capacity is 274 mAh/g, both an order of magnitude lower than the 3861 mAh/g capacity for Li metal. As an aside, there is a reasonable, but somewhat misleading convention in the literature to express the theoretical capacity based on the weight of the material that goes into the battery construction instead of at a standardized state of charge. $\text{Li}_y\text{C}_6/\text{Li}_{1-x}\text{CoO}_2$ cells are constructed in the discharged state with $y = 0$, and the reported theoretical capacity for the graphite anode thus neglects the contribution of the Li ions to the electrode mass. While this is not in general a large effect, it is important to note since the reported theoretical capacity of a material may vary based on its charge state during battery construction.

Although Li intercalation cathodes including LiCoO_2 were known in the late 1970s,⁵ and work on Li intercalated graphite took place even earlier,⁶ Li-ion batteries did not experience commercial success until the early 1990s. In large part this gap was due to considerable difficulty in identifying successful electrolyte materials. Li salts are soluble in several low viscosity organic solvents, but in general these solvents were not stable with respect to the electrode materials. Early solvents such as propylene carbonate decomposed graphite electrodes,⁶ and reactivity with the electrolyte also plagued cells with Li metal electrodes. Safety concerns due to Li metal/electrolyte reactions resulted in a 1989 recall of an early commercial lithium battery after several batteries caught fire.⁷

Finding a stable electrolyte has always been particularly vexing for lithium batteries. Most other rechargeable batteries use aqueous electrolytes, which have an electrochemical stability window of approximately 1.3 V. Li-ion cells using aqueous electrolytes can also be constructed, but only at the cost of a dramatically reduced cell voltage, with a corresponding loss of energy density.⁷ The voltage relative to Li metal for LiC_6 is approximately 0.2 V, nearly as low as metallic Li itself, while the potential associated with LiCoO_2 is about 4.0 V. In both cases the voltage varies slightly depending on state of charge. While the 3.8 V potential difference in the $\text{Li}_y\text{C}_6/\text{Li}_{1-x}\text{CoO}_2$ cell is advantageous for energy storage, it poses difficulty for electrolyte materials.

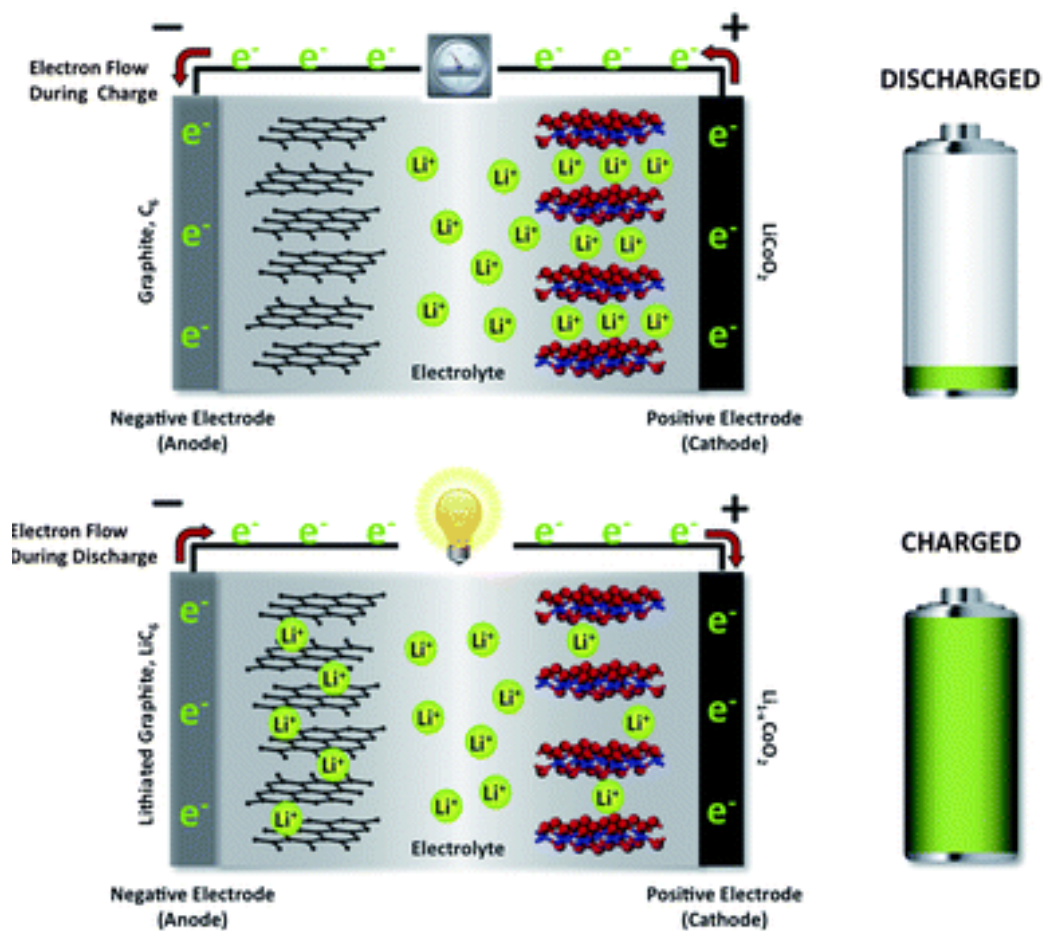


Figure 1.2: Li-ion battery shown in both the charged and discharged state. The intercalation of the Li between the sheets of both graphite and $LiCoO_2$ can be clearly seen. The existence of intercalated Li in the cathode even when fully charged reflects the instability of $LiCoO_2$ below a certain level of lithiation. Adapted from reference 4 with permission of the Royal Society of Chemistry.

The most common class of Li-ion electrolytes are liquid carbonates, with an ionic conductivity of 10mS/cm.⁸ These organic solvents such as propylene carbonate, ethyl carbonate, diethyl carbonate and dimethyl carbonate have 3.7 V stability windows, with their LUMO and HOMO levels located at approximately 1 V and 4.7 V respectively.⁹ The voltages for both graphite and Li metal are thus well below the start of the stability window for these electrolytes, and the unsuitability of propylene carbonate for graphite electrodes was already referenced above. In spite of this fact, liquid carbonate electrolytes were not only used in early commercial Li batteries, but remain the dominant electrolyte chemistry. This dominance is possible because while the carbonate electrolytes are reduced by the anode, in cells with graphite anodes and electrolytes comprised of mixtures of ethyl and diethyl carbonate this reduction reaction forms a self-limiting passivating layer known as the solid electrolyte interphase (SEI).

The formation of an SEI results in irreversible capacity loss, and once formed the layer interferes with ionic conductivity, thereby increasing the internal resistance and decreasing the maximum charge rate of the battery. SEI layers also form in Li metal cells, however, the Li electrode undergoes significant volume changes during charge and discharge. These break the passivating layer and cause additional capacity loss. Graphite anodes on the other hand have a much more modest variation in volume of only 10%. This modest expansion allows the SEI formed during the initial charging of the battery to better passivate the electrode.

In addition to SEI formation, the other downside of the organic carbonate electrolytes is that they are the largest safety concern in Li batteries. The primary source of concern is that the electrolytes are highly flammable. In addition to the early recall that ended work on commercializing batteries with Li metal anodes, Li-ion battery fires have affected laptop computers, electric cars, and commercial airliners. Current Li-ion battery design thus requires a large focus on safety, which is primarily due to the lack of inherent safety in the electrolyte. Most Li-ion batteries contain microelectronic circuits that help to regulate charging and prevent overcharging the cell, since overcharge accelerates SEI formation.¹⁰ Additional safety measures are incorporated into battery packs for the large format cells used in electric vehicles and aerospace applications.

In summary, Li batteries typically exhibit a relatively high energy density, in part due to the large voltage differences between their electrodes. They have relatively poor safety performance due to overheating and flammability concerns. The formation of a stable SEI for the graphite anode allows them fairly good cycle life, provided slow charging speeds.

1.4 Near term: promising research directions

There are several promising directions for Li battery research including the development of higher voltage cathodes, the use of single element electrode chemistries like S, Si, and Li metal to give order of magnitude increases in capacity, and a significant research effort towards nano-engineered battery structures. While the field of

Li-ion batteries has developed enormously in the last 35 years, In many ways Li-ion batteries today face the same problem they faced in the 1980s, the instability of the electrolyte/electrode interface.

Higher voltage and lower cost cathode materials have been created, both by modifying the LiCoO_2 material via partial substitution of Mn or Ni for Co, or by the discovery of wholly novel compounds. For many of these high voltage cathodes, their electrode voltage exceeds the electrochemical stability window of the electrolyte. While work continues on these systems, until a better electrolyte is developed there is no practical application.

Lithium-sulfur batteries combine two electrodes with an order of magnitude greater capacity than current cells, but the Li-S reaction products are soluble in carbonate electrolytes. In addition to the existing issues with combining metallic Li and liquid electrolytes, the Li-S cathode is also unstable with respect to current electrolyte materials.

An enormous amount of engineering goes into making Li batteries relatively safe, and the vast majority of that danger is due to the flammability of the electrolyte. The fear of thermal runaway and catastrophic failure almost killed the Li battery in the 1980s, and it continues to be a drag on battery development.

While it is impossible to know the future, replacing organic liquid electrolytes with high conductivity inorganic solids is probably the most promising research direction for improving Li batteries. In addition to strong academic interest, the Toyota Motor Corporation, which has approximately a 50% market share of the American hybrid electric vehicle market, has claimed that it expects superior solid-state Li batteries to be developed in the next five years.¹¹

In liquid electrolyte cells, Li metal is not considered a practical electrode material despite its high theoretical capacity because during charge cycling metallic Li grows dendrites. Small protuberances at the surface of the Li electrode have stronger electric fields associated with them than the surface and attract Li^+ ions in the charging battery. The attracted ions cause the protuberances to grow, forming small, tree-like whiskers called dendrites. If these whiskers cross the electrolyte, the battery can develop internal sparking and can also short circuit and overheat.

Solid electrolytes materials on the other hand suppress the growth of Li dendrites, and Li metal anodes are used in solid electrolyte batteries in the thin film configuration. Solid electrolytes with high enough conductivities for power battery applications potentially enable the use of Li metal as an anode material, which represents an order of magnitude increase in electrode capacity.

Solid electrolyte materials traditionally have wide electrochemical windows, which is why they are viewed as an important technology for high voltage cathodes.¹² The primary downside of Li solid electrolytes is that they historically have relatively low ionic conductivity. However, in recent years several lithium thiophosphate solid electrolytes related to Li_3PS_4 with conductivities approaching and even exceeding that of the liquid carbonates have been developed.^{13,14}

There is thus a strong incentive to explore and characterize potential solid electrolytes, especially those related to the Li_3PS_4 system. Electrolyte materials have two primary functional properties, the transport of ions across the cell and the formation

of stable interfaces with the electrodes. The theoretical methods for determining the ionic conductivity of solid electrolyte materials appear to be fairly well-established and of comparable precision to experimental methods.¹⁵ The characterization of solid-solid interfaces in battery materials is by comparison, critically understudied.

The specific research question addressed in this work is thus the further development of a theoretical procedure for characterizing solid-solid electrode/electrolyte interfaces based on first principles density functional theory simulations. These methods are then applied to the study of $\text{Li}_3\text{PS}_4/\text{Li}$ interfaces and several related systems.

Chapter 2

Computational Theory

[T]here is no choice but to suspend disbelief and begin to calculate

Michael Marder

2.1 Quantum mechanics

While materials can be modelled at several different length scales, most of the properties relevant to battery materials depend on the movement of electrons and small ions and are most tractably described using quantum mechanics. In principle, a full quantum mechanical model of a material could be arrived at by solving the time independent Schrödinger equation

$$H|\Psi\rangle = E|\Psi\rangle \tag{2.1}$$

where H is the Hamiltonian of the system, Ψ is the wavefunction, and E is the total energy.

The central focus of this chapter is to briefly describe how practical solutions to equation 2.1 were obtained for the systems studied in this work. This explication is intended to be illustrative rather than comprehensive. A discussion of quantum mechanical phenomena such as degenerate eigenstates and spin degrees of freedom that slightly complicate the presentation without altering the fundamental results is omitted. Similarly, while several alternative approaches to the one presented here for solving equation 2.1 exist, the sheer variety of techniques precludes a serious discussion of the relative merits of the many methods.

Solutions for equation 2.1 for model systems like the harmonic oscillator, can often be found analytically. For most realistic systems, Ψ is a function of many variables, and the only feasible approach is numerical optimization methods. Optimization methods rely on evaluating possible solutions based on their performance against some objective function. In this instance, the total energy itself serves as the objective function due to the variational principle.

The variational principle states that for a quantum mechanical system with Hamiltonian H and ground state energy E_{gs} , for all possible trial wavefunctions Φ the expectation value of the energy must always be greater than or equal to E_{gs}

$$E_{gs} \leq \frac{\langle \Phi | H | \Phi \rangle}{\langle \Phi | \Phi \rangle}. \quad (2.2)$$

The set of eigenfunctions of H form a complete basis and any normalized trial wavefunction can be represented as a linear combination of those eigenfunctions. If Ψ_n represents the n th eigenfunction of H such that Ψ_0 is the true ground state wavefunction (i.e. the eigenfunction of H with the smallest eigenvalue) then the energy $\langle \Phi | H | \Phi \rangle$ can always be expressed by a sum on n of $\langle \Psi_n | H | \Psi_n \rangle$. If $\Phi = \Psi_0$ then Φ is the true ground state wavefunction and the equality $\langle \Phi | H | \Phi \rangle = E_{gs}$ holds. Otherwise, Φ contains contributions from higher energy eigenstates and the inequality $E_{gs} < \langle \Phi | H | \Phi \rangle$ holds.

While the variational principle makes the optimization of trial wavefunctions possible, several approximations are necessary before such optimization is practical for the systems that describe battery materials. The approximations covered here are the Born-Oppenheimer approximation, and the independent electron approximation, all of which are explained within the context of Kohn-Sham density functional theory.

2.2 Born-Oppenheimer approximation

The general form of the Hamiltonian operator for a system comprised of a mixture of electrons and atomic nuclei is

$$H = \sum_A \frac{-\hbar^2 \nabla_A^2}{2M_A} + \sum_i \frac{-\hbar^2 \nabla_i^2}{2m_e} - \sum_{A,i} \frac{e^2 Z_A}{|\vec{R}_A - \vec{r}_i|} + \frac{1}{2} \sum_{A,B \neq A} \frac{e^2 Z_A Z_B}{|\vec{R}_A - \vec{R}_B|} + \frac{1}{2} \sum_{i,j \neq i} \frac{e^2}{|\vec{r}_i - \vec{r}_j|}. \quad (2.3)$$

In this expression the lower case subscripts represent sums over the electrons and upper case subscripts correspond to sums over the atomic nuclei. The mass of the nuclei is denoted with M_A ; the electron mass is m_e ; e is the fundamental charge; and Z_A represents the atomic number. The first term corresponds to the nuclear kinetic energy, the second represents the electronic kinetic energy, the third term is due to the energy of the nuclear-electronic interaction, and the final two terms represent the ion-ion and electron-electron interactions respectively.

The purpose of the Born-Oppenheimer approximation is to decouple the nuclear and electronic degrees of freedom. This decoupling is well-justified by the substantial difference between the mass of the electron and that of the proton and neutron, $m_{proton} \approx m_{neutron} \approx 1840m_e$. An electron that exerts a force on one of the atomic nuclei experiences an equal and opposite force in accordance with the conservation of momentum. The resulting change in the kinetic energy of the much lighter electron will be thousands of times larger than the change in the nuclear kinetic energy. For

the purpose of determining the electronic structure of a material the nuclear kinetic energy term, $\frac{-\hbar^2 \nabla_A^2}{2M_A}$, can thus be safely neglected.

The insignificance of the nuclear kinetic energy is equivalent to the statement that the nuclei move very slowly relative to the electrons. The slow movement of the nuclei justifies the adiabatic approximation, where the nuclear positions are assumed to be evolving slowly enough that they can be taken as constants for determining the electronic structure. From the perspective of the electrons these stationary ions can be described as a fixed external potential $v(\vec{r})$ represented by the operator V_{ext} .

Finally, the ion-ion interaction term does not affect the electronic wavefunction at all, and the sum over ions in the fourth term can be evaluated and replaced by a constant. This constant affects the total energy, but has no effect on the eigenstates of the Hamiltonian.

The electronic Hamiltonian for a system of N electrons can thus be written as

$$H = \sum_{i=1}^N \frac{-\hbar^2 \nabla_i^2}{2m_e} + \frac{1}{2} \sum_{i=1, j \neq i}^N \frac{e^2}{|\vec{r}_i - \vec{r}_j|} + V_{ext} \quad (2.4)$$

$$= T + V_{ee} + V_{ext} . \quad (2.5)$$

2.3 Hohenberg-Kohn theorem

While the Born-Oppenheimer approximation reduces the difficulty of finding electronic eigenstates of equation 2.3, the problem remains intractable. Equation 2.4 has eigenstates that depend on the position of each of the N electrons in the system, $\Psi(\vec{r}_1, \vec{r}_2, \vec{r}_3, \dots, \vec{r}_N)$. While equation 2.2 provides an objective function suitable for numerical optimization techniques, Ψ is a function of $3N$ variables and locating the correct wavefunction in such a vast space of possibilities is prohibitively difficult.

Although Ψ depends on the positions of N electrons, the electrons themselves are identical. Because of this, the first two terms of the Hamiltonian defined in equation 2.4 are unchanged for any N electron system; only the V_{ext} term varies from system to system. All of the observed variation in ground state electronic structure must somehow be represented in the V_{ext} term.

The energy of for the wavefunction of a set of N electrons interacting only with the V_{ext} operator is given by the expression

$$\langle \Psi | V_{ext} | \Psi \rangle = \int \langle \Psi(\vec{r}'_1, \vec{r}'_2, \dots, \vec{r}'_N) | \sum_{i=1}^N \delta(\vec{r} - \vec{r}'_i) v(\vec{r}) | \Psi(\vec{r}'_1, \vec{r}'_2, \dots, \vec{r}'_N) \rangle d\vec{r} \quad (2.6)$$

$$= \int n(\vec{r}) v(\vec{r}) d\vec{r} , \quad (2.7)$$

where $n(\vec{r})$ is the electron density and $v(\vec{r})$ is the external potential. The inner product in equation 2.6 represents integration over all N of the \vec{r}'_i coordinates. Since T and V_{ee} do not depend on the system, the choice of V_{ext} determines the Hamiltonian, and consequently the eigenstates and the ground state electronic density.

It is worth investigating whether the mapping from the external potential V_{ext} to the electronic density is injective, i.e. a one-to-one function. Consider the contradiction, that there exist two external potentials v_1 and v_2 with corresponding Hamiltonians H^1 and H^2 , ground state wavefunctions Ψ^1 and Ψ^2 , and electronic densities n_1 and n_2 such that $V_1 \neq V_2$ and $n_1(\vec{r}) = n_2(\vec{r}) = n(\vec{r})$.

The variational principle guarantees that

$$E_1 = \langle \Psi^1 | H^1 | \Psi^1 \rangle < \langle \Psi^2 | H^1 | \Psi^2 \rangle , \quad (2.8)$$

from which it follows that

$$E_1 < \langle \Psi^2 | H^1 - H^2 | \Psi^2 \rangle + \langle \Psi^2 | H^2 | \Psi^2 \rangle . \quad (2.9)$$

Because the T and V_{ee} terms in H^1 and H^2 are identical, this simplifies to

$$E_1 < E_2 + \int n(\vec{r})[v_1(\vec{r}) - v_2(\vec{r})]d\vec{r} . \quad (2.10)$$

However, an identical argument can be made concerning E_2 , so that

$$E_2 < E_1 + \int n(\vec{r})[v_2(\vec{r}) - v_1(\vec{r})]d\vec{r} . \quad (2.11)$$

Adding together equations 2.10 and 2.11 gives the contradiction

$$E_1 + E_2 < E_2 + E_1 . \quad (2.12)$$

Because V_{ext} determines the Hamiltonian and the ground state wavefunction, but is itself uniquely determined by $n(\vec{r})$ it must be true that the entire Hamiltonian can be written as a functional of the electron density. Combining this result with equation 2.4 gives the relation

$$E[n] = T[n] + V_{ee}[n] + \int n(\vec{r})v(\vec{r})d\vec{r} , \quad (2.13)$$

where $T[n]$ and $V_{ee}[n]$ now denote the expectation values of the kinetic energy and electron-electron interaction operators. As a notational aside, the distinction between operator and expectation value throughout this chapter is indicated by this usage of square brackets.

Equation 2.13 is known as the Hohenberg-Kohn theorem. The advantage of writing the energy in this form is that $n(\vec{r})$ is a function of only 3 dimensions, and expressing the energy as a functional of the density thus avoids the exponentially huge search space associated with treating Ψ as the variational parameter. The injective mapping between the ground state wavefunction $\Psi_{gs}(\vec{r}_1, \dots, \vec{r}_N)$ and $n(\vec{r})$ guarantees that the variational principle applies to $n(\vec{r})$ and that the correct $n(\vec{r})$ is the one that minimizes the energy. This method is aptly referred to as density functional theory (DFT).

2.4 Independent electron approximation

The Hohenberg-Kohn theorem cleverly circumvents the difficulty associated with the exponentially large search space for the wavefunction, but equation 2.13 is still not a practical relation for most materials. This is primarily because the kinetic energy operator T is not readily expressed as a functional of the density. The density contains contributions from many particles, but T is a sum over partial derivatives with respect to the positions of particular electrons. Since the kinetic energy of the electrons represents a large portion of the total energy of almost all systems, a method to estimate $T[n]$ is necessary.

The Kohn-Sham approach,¹⁶ similar to the approach taken in Hartree-Fock theory, attempts to replace the interacting many-body problem with a model system based on non-interacting single particle states. The fundamental assumption of Kohn-Sham theory is that the ground state density that minimizes equation 2.13 can be expressed in terms of single particle states according to the relation

$$n(\vec{r}) = \sum_{i=1}^N |\psi_i(\vec{r})|^2 . \quad (2.14)$$

Writing the density this way makes it easy to write down a functional form for the expectation value of the kinetic energy operator

$$T_I[n] = \frac{1}{2m_e} \sum_{i=1}^N \int d\vec{r} |\hbar \nabla \psi_i(\vec{r})|^2 . \quad (2.15)$$

Because the states are orthonormal, the sum over i in equation 2.4 has been combined with the sum over i in equation 2.14. This value is denoted $T_I[n]$ to differentiate the kinetic energy in the independent electron approximation from the many-particle kinetic energy $T[n]$.

In the independent electron approximation the sum over individual particles in the definition of V_{ee} becomes an integral over the average electron density, and V_{ee} is replaced by a new operator $E_{Hartree}$ that describes the interaction of the electron density with itself according to the equation

$$E_{Hartree}[n] = \frac{e^2}{2} \int \frac{n(\vec{r})n(\vec{r}')}{|\vec{r} - \vec{r}'|} d\vec{r} d\vec{r}' . \quad (2.16)$$

While these approximations enable equation 2.13 to be evaluated, there are obvious issues. For a system with only a single electron $\langle \Psi | V_{ee} | \Psi \rangle$ should be zero, but $E_{Hartree}$ will not be. Similarly, while T_I and $E_{Hartree}$ are supposed to represent the electron-electron interaction, neither term includes the effect of the Pauli exclusion principle. In order to recover some of the lost physics an error term called the exchange-correlation functional $E_{xc}[n]$ can be defined by

$$E_{xc}[n] = T[n] - T_I[n] + V_{ee}[n] - E_{Hartree}[n] . \quad (2.17)$$

This enables equation 2.13 to be rewritten, without loss of accuracy as

$$E_{KS}[n] = T_I[n] + E_{Hartree}[n] + \int n(\vec{r})v(\vec{r})d\vec{r} + E_{xc}[n] . \quad (2.18)$$

Equation 2.18 is not obviously an improvement over equation 2.13 since the unknown functional $E_{xc}[n]$ depends in principle on both of the unknown functionals $T[n]$ and $V_{ee}[n]$, but physically meaningful approximations as a functional of the density are easier to create for $E_{xc}[n]$ than for $T[n]$. Under this approach, $T_I[n]$ is a reasonably good approximation of $T[n]$ and the single particle Kohn-Sham states needed to determine $T_I[n]$ can be arrived at by solving the Hamiltonian implied by equation 2.18

$$\left(\frac{-\hbar^2}{2m_e} \nabla^2 + \frac{e^2}{2} \int \frac{n(\vec{r}')}{|\vec{r} - \vec{r}'|} d\vec{r}' + v(\vec{r}) + V_{xc} \right) \psi_i = E\psi_i . \quad (2.19)$$

The only term in this equation not already defined is the exchange-correlation potential, V_{xc} , given by the functional derivative of $E_{xc}[n]$ with respect to the density. While the true functional form of this operator is unknown, the two most well-known approximate forms of V_{xc} are the local density approximation (LDA),¹⁷ which evaluates $E_{xc}[n]$ using an integral over the local electron density, and the generalized gradient approximation (GGA),¹⁸ which expresses $E_{xc}[n]$ as a function of both the electron density and its spatial derivative.

Chapter 3

Interfaces Between Crystalline Materials

3.1 Conceptual overview

For a given interface, its configuration Ω can be described in terms of the positions of all of the atoms that make up the interface. Among the innumerable possibilities for the interface configuration Ω between materials a and b , there are three broad classifications based on the extent to which the lattices of the two materials align.^{19,20} A coherent interface exhibits nearly perfect compatibility between the lattice constants of the two materials at the interface, and the lattice planes are continuous across the interface. The resulting interface structure can be described by a single periodic phase, with periodicity set by the lattice constants of the composite system. At a semi-coherent interface, the two materials have similar but not equal lattice spacing, which results in lattice strain at the interface. In order to relieve this strain, semi-coherent interfaces typically involve defect sites at the interface, so that not all of the lattice planes are continuous across the interface boundary. For an incoherent interface, there is significant mismatch between the lattice constants of the two materials, and there is no significant continuity of lattice planes across the interface.

A number of energetic measures to characterize interfaces have been defined in the literature.^{19–26} The interface energy (γ_{ab}) between materials a and b is defined as the energy difference between an interface system and the bulk energy of the two materials that comprise it for a given Ω .

$$\gamma_{ab}(\Omega) = \frac{E_{ab}(\Omega, A, n_a, n_b) - n_a E_a - n_b E_b}{A}. \quad (3.1)$$

Here, E_{ab} denotes the total energy of the complete system containing the interface, and it depends on how many formula units of materials a and b comprise the interface (n_a and n_b respectively), as well as on the configuration Ω and the interfacial area A . E_a and E_b denote the bulk energy per formula unit for materials a and b respectively. Another energy measure is the ideal work W_{ab} of adhesion or separation^{21,23} which

models the idealized separation of the interface into two surfaces in vacuum.

$$W_{ab}(\Omega) = \gamma_{a,vac}(\Omega) + \gamma_{b,vac}(\Omega) - \gamma_{ab}(\Omega). \quad (3.2)$$

In this expression $\gamma_{a,vac}(\Omega)$ and $\gamma_{b,vac}(\Omega)$ denote the ideal surface energies of materials a and b in vacuum for the particular cleavages implied by the configuration Ω .

Ω depends on the positions of all of the atoms at the interface and includes not only the detailed geometries, but also the effects of cleavage planes, interface alignment, and defect structures produced by lattice mismatch. There are, in principle, many possible interface configurations, but in practice we expect likely interfaces to exhibit both relatively low interface energies and local order approximately consistent with either the bulk ordering of material a or with that of material b , or with both. While there may not be a single value of γ_{ab} for two materials, by sampling likely configurations Ω we can establish both a likely value for γ_{ab} and an estimate for the range of its variation.

Because γ_{ab} is an intensive energy, it can in principle be computed by determining the γ_{ab} values of successively larger subregions of the interface using the convergence of the limit

$$\lim_{\Omega_s \rightarrow \Omega} [\gamma_{ab}(\Omega_s)] = \gamma_{ab}(\Omega), \quad (3.3)$$

where Ω_s denotes the atomic configuration in some sample interface volume. Because Ω may exhibit periodic structure on a variety of different length scales,¹⁹ $\lim_{\Omega_s \rightarrow \Omega} [\gamma_{ab}(\Omega_s)]$ is not monotonic and correctly computing this limit requires careful consideration of possible interface structures, especially dislocation defects caused by lattice mismatch between the two interface materials.

3.2 Interface formalism

While the definition of the interface energy given in Eq. (3.1) is fully general, it is prohibitively expensive to evaluate the energy for a given trial configuration Ω and difficult even to satisfactorily converge the sampling limit Ω_s . In the interest of efficiency, instead we consider approximate interface configurations Ω that correspond to periodic ordered phases we label $\tilde{\Omega}$. In the case of a coherent interface, where there is no mismatch between the lattices of the interface materials the interface phase described by Ω is automatically periodic and $\tilde{\Omega}=\Omega$.

The more likely case is that of the semi-coherent interface, where there is some degree of lattice mismatch between the two phases. By imposing periodic boundary conditions to the simulation system, a lattice strain is necessarily introduced into the system to bring the two lattices into alignment. This strain energy scales with the amount of material under strain and can be assumed to have the functional form $\tilde{E}_{str}(\tilde{\Omega}, n_a, n_b)$. Consequently, while we can still define an interface energy according to Eq. (3.1), it is no longer an intensive quantity; the interface energy calculated in the periodic cell now depends on n_a and n_b

$$\tilde{\gamma}_{ab}(\tilde{\Omega}, n_a, n_b) = \frac{\tilde{E}_{ab}(\tilde{\Omega}, A, n_a, n_b) - n_a E_a - n_b E_b}{A}. \quad (3.4)$$

The terms of this equation are defined identically to those in Eq. 3.1, although for clarity we label the quantities computed in our periodic cell with a tilde. Because of the periodic boundary conditions, each simulation cell contains two interfaces and the area A represents the combined area of both. Correspondingly, $\tilde{\gamma}_{ab}(\tilde{\Omega}, n_a, n_b)$ is the average of the two interface energies. Because of the lattice strain, $\tilde{\gamma}_{ab}$ does not converge with respect to system size in the direction perpendicular to the interface. For the true interface configuration Ω , the strain is relieved by the formation of dislocation defects so the strain energy $\tilde{E}_{str}(\tilde{\Omega}, n_a, n_b)$ present in $\tilde{\gamma}_{ab}$ is unphysically large.

Subtracting the strain energy from $\tilde{\gamma}_{ab}$ is equivalent to calculating the interface energy in the coherent limit, and is given by the equation

$$\begin{aligned} \tilde{\gamma}_{ab}^{lim}(\tilde{\Omega}) &= \tilde{\gamma}_{ab}(\tilde{\Omega}, n_a, n_b) - \frac{\tilde{E}_{str}(\tilde{\Omega}, n_a, n_b)}{A} \\ &= \frac{\tilde{E}_{ab}(\tilde{\Omega}, A, n_a, n_b) - n_a E_a - n_b E_b - \tilde{E}_{str}(\tilde{\Omega}, n_a, n_b)}{A}. \end{aligned} \quad (3.5)$$

In this equation, \tilde{E}_{str} denotes the strain energy, A is the area of the interface, $\tilde{\Omega}$ the interface configuration in the periodic cell, n_a and n_b represent the number of formula units of materials a and b , and E_a and E_b represent the energy per formula unit of the two materials in their unstrained bulk configurations. As an aside, we note that instead of the explicit inclusion of a strain energy term, some authors replace the E_a and E_b terms with the energy per formula unit in the strained bulk.^{22,23} Unlike $\tilde{\gamma}_{ab}(\tilde{\Omega}, n_a, n_b)$, $\tilde{\gamma}_{ab}^{lim}(\tilde{\Omega})$ does not depend on n_a or n_b , and thus converges much better with respect to system size and provides a better estimate of $\gamma_{ab}(\Omega)$. Similar ideas were previously discussed by Benedek et al.²⁰

The definition of $\tilde{\gamma}_{ab}^{lim}(\tilde{\Omega})$ assumes that the interface interaction has a finite range and that beyond some threshold value of n_a or n_b additional formula units of material a or b only affect the strain energy. \tilde{E}_{str} can be determined in multiple ways, but the approach taken in this work exploits the dependence of both $\tilde{\gamma}_{ab}$ and \tilde{E}_{str} on the system size. We calculated $\tilde{\gamma}_{ab}$ for several interface systems which had the same interface configuration $\tilde{\Omega}$ and had their lattices fixed to the bulk values of material a , but which had different amounts of material b . Because the lattice constants for the interface system are fixed to the values of material a , \tilde{E}_{str} depends only on n_b . For these systems beyond the threshold value of n_b Eq. 3.5 can be rearranged to obtain the relation

$$\tilde{\gamma}_{ab}(\tilde{\Omega}, n_b) = \tilde{\gamma}_{ab}^{lim}(\tilde{\Omega}) + n_b \sigma \quad (3.6)$$

where σ is a constant related to the strain energy in material b . This approach both enables an explicit treatment of the strain energy and makes the results less sensitive to possible phase changes in material b due to the combined effects of the interface and interface strain. Plotting $\tilde{\gamma}_{ab}(\tilde{\Omega}, n_b)$ against n_b yields a straight line with slope σ and intercept $\tilde{\gamma}_{ab}^{lim}(\tilde{\Omega})$.

It is important to note that because $\tilde{\gamma}_{ab}^{lim}(\tilde{\Omega})$ does not contain the energy contributions from defect sites, it is an underestimate of the true interface energy $\gamma_{ab}(\Omega)$. The

real interface energy will fall between $\tilde{\gamma}_{ab}^{lim}$ and $\tilde{\gamma}_{ab}$. For coherent and semi-coherent cases where $\tilde{\Omega} \approx \Omega$ this gives the relation

$$\tilde{\gamma}_{ab}^{lim}(\tilde{\Omega}) \leq \gamma_{ab}(\Omega) \leq \tilde{\gamma}_{ab}(\tilde{\Omega}, n_a, n_b) \quad (3.7)$$

with the equalities corresponding to the coherent case. The difference between $\tilde{\gamma}_{ab}$ and $\tilde{\gamma}_{ab}^{lim}$ can thus provide an error bound for the difference between the true interface energy and the energy calculated in the coherent limit. This error bound provides an estimate of the error associated with the limited in-plane size of the periodic supercell approximation of the interface, i.e., the in-plane lattice supercell error.

Part II
Novel Results

Chapter 4

Methods

4.1 Basic

The computational methods are based on Kohn-Sham density functional theory^{16,27} as described in Chapter 2 and implemented in the Quantum Espresso software package.²⁸ Pseudopotentials were constructed within the projector augmented wave formalism,²⁹ and the associated basis and projector functions were generated using the Atompaw code.³⁰

The exchange-correlation functional was chosen to be the local density approximation,¹⁷ consistent with earlier results that demonstrated the accuracy of that choice for the solid electrolyte systems I consider.³¹ The Bloch wavefunctions were well-converged within a plane wave cutoff of 64 Rydbergs. The Brillouin zone was sampled using the Monkhorst-Pack grid scheme with a typical grid volume of 0.02 \AA^{-3} or smaller and Gaussian smearing of 0.001 Ry.

Partial densities of states were computed from weight factors for each state approximating the electron density within the augmentation sphere about each atomic site and then averaged over atomic sites within a given set s . Explicitly, the partial density of states for a set of atomic sites s is given by

$$N^s(E) = \frac{1}{M_s} \sum_{a \in s} N^a(E) \quad \text{where} \quad (4.1)$$
$$N^a(E) = \left(\sum_{n\mathbf{k}} W_{\mathbf{k}} Q_{n\mathbf{k}}^a \delta(E - E_{n\mathbf{k}}) \right),$$

where the M_s denotes the number of atoms a in set s and $W_{\mathbf{k}}$ denotes the Brillouin zone weighting factor for approximating the Brillouin zone integration. The factor $Q_{n\mathbf{k}}^a$ is given by the charge within the augmentation sphere of atom a for state $n\mathbf{k}$.

$$Q_{n\mathbf{k}}^a \approx \sum_{ij} \langle \tilde{\Psi}_{n\mathbf{k}} | p_{n_i l_i m_i}^a \rangle \langle p_{n_j l_j m_j}^a | \tilde{\Psi}_{n\mathbf{k}} \rangle q_{n_i l_i; n_j l_j}^a \delta_{l_i l_j}, \quad (4.2)$$

in terms of the radial integrals

$$q_{n_i l_i; n_j l_j}^a \equiv \int_0^{r_c^a} dr \varphi_{n_i l_i}^a(r) \varphi_{n_j l_j}^a(r). \quad (4.3)$$

In these relations $|\tilde{\Psi}_{n\mathbf{k}}\rangle$ refers to the pseudo-wavefunction, while $|\tilde{p}_{n_i l_i m_i}^a\rangle$ corresponds to the atomic projector function within the augmentation sphere about the atomic site a . The indices $n_i l_i m_i$ denote radial and spherical harmonic indices of the projector function.^{29,32} $\varphi_{n_i l_i}^a(r)$ represents an all-electron radial basis function. The specific augmentation radii used in this work are $r_c^{\text{Li}} = 1.6$, $r_c^{\text{O}} = 1.2$, $r_c^{\text{P}} = 1.7$, and $r_c^{\text{S}} = 1.7$ in Bohr units. In practice, the δ function is represented by a Gaussian smoothing function with a width of 0.14 eV. The k-point sampling for evaluating the partial densities of states was typically eight times denser than that used for the structural optimization studies and in some cases was further increased in order to generate smoother curves.

The “nudged elastic band” (NEB) method,^{33–35} as programmed in the *QUANTUM ESPRESSO* package was used to estimate activation energies. In order to increase the stability of the NEB path finding algorithm, the movements of atoms uninvolved in the modelled migrations had artificial costs imposed on them.

Because of the usage of periodic boundary conditions, for surface systems that contained a net dipole, the effect of the periodic image dipole-dipole interaction was removed using a compensating fictitious charge distribution in the vacuum region.³⁶ Visualizations of the supercell configurations were constructed using the *XCryS-DEN*^{37,38} and *VESTA*³⁹ software packages.

4.2 Interface representations

Supercells constructed with alternating sections of material a and material b were used to evaluate the interface energy as defined in equations (3.4) and (3.6). For the interfaces considered in this study, I chose the electrolytes as material a , which means that the supercell lattice constants were fixed in accordance with equation 3.6 to their calculated bulk values. The slab geometry and periodic boundary conditions resulted in the formation of two a - b interfaces in each simulation cell, and for most systems the interfaces were constructed to be symmetrically equivalent.

In order to observe the linear relationship implied by equation (3.6), I constructed sets of supercells with a fixed interface configuration $\tilde{\Omega}$ and a varying number of layers of material b . Possible interface configurations were discovered by optimizing both the atomic positions and the supercell lattice constant normal to the interface of trial structures. Because the number of possible configurations is large and because the relaxation algorithm only discovers local minima, I started the optimization from several globally distinct initial configurations to better sample the configuration space. These initial configurations were generated in several ways over the course of this study.

One approach common in the literature is to choose surface planes for materials a and b with similar lattice constants in order to construct a supercell with minimal lattice mismatch at the interface. While I followed this approach for many of my interface systems, of the reported configurations, only the $\text{Li}_3\text{PS}_4/\text{Li}_2\text{S}$ interface configuration was determined using this method alone.

One limitation of this approach is that the high degree of order in the initial con-

figuration limits the ability of the optimization algorithm to find interface structures that differ significantly from the initial guess. Determining likely trial structures for Li metal in particular is complicated by the existence at low temperature of several bulk phases with very similar energies.^{40,41} As a consequence, a naively constructed sequence of Li structures can not only fail to adequately sample the configuration space, but also result in Li metal slabs that contain defects and heterogeneous phases.

In one attempt to address this difficulty, I constructed initial Li configurations using orthorhombic grids with a structure based on that of Li monolayers. The relaxation algorithm tended to preserve the symmetry of the grid and the resulting configurations $\tilde{\Omega}$ exhibited relatively large strain parameters σ . I also generated initial configurations by adding random noise to the positions of atoms in ordered Li structures before optimizing the interface. Applying this method to a relatively small number of Li atoms, generally resulted in an ordered Li structure which was less sensitive to the initial guess and which could be systematically extended along the interface normal direction to generate slabs of varying thicknesses.

The results presented below all follow the approach described by equation (3.6) based on a series of three or more consistent supercell simulations. These results were corroborated by additional simulations using larger supercells and additional configurations.

Chapter 5

Li₂O/Li System

5.1 Li₂O/Li interfaces

Li₂O is a good candidate material because of its stability with respect to Li and its relatively simple crystal structure, shown in Figure 5.1. Additionally, the choice of Li₂O enables comparison with earlier works, as the interface between Li₂O and Li metal has been well-characterized in the literature.⁴²⁻⁵⁰ In this work I focus on interfaces with the non-polar (110) surface of Li₂O. I considered multiple interface configurations $\tilde{\Omega}$, and two representative cases are depicted in Figure 5.2. In general I found that beyond three layers, the dependence of the results on the total number of electrolyte layers was negligible, although the number of layers does affect the symmetry of the resulting slab. Depending on the Li slab symmetry, the number of electrolyte layers had to be adjusted in order to maintain symmetric interfaces within the cell, as illustrated by the geometries shown in Figure 5.2.

The calculated lattice constant for Li₂O ($Fm\bar{3}m$) in my simulations was 4.53 Å. For both of the reported configurations the supercell geometry is an orthorhombic cell with lattice constants equal to 4.53 Å in the [100] direction and 6.31 Å in the [1-10] direction. The lattice constant in the [110] direction depends on the amount of metallic Li in the simulated system.

For the interface labeled Li₂O/Li($\tilde{\Omega}_1$) the metallic Li structure is patterned after the Li structure within Li₂O, as illustrated in Figure 5.2(a). The interface labeled Li₂O/Li($\tilde{\Omega}_2$), shown in Figure 5.2(b), is representative of several similar interfaces whose Li positions were derived from optimizing an initial configuration generated by adding around one Å of random noise to the Li metal positions in the $\tilde{\Omega}_1$ struc-

Table 5.1: Li₂O Data Table

Symmetry	$Fm\bar{3}m$ (#225)
Calc. Lattice (Å)	4.53 Å
Formula Units/Conventional Cell	4
Formation Enthalpy/Formula Unit	-6.10 eV
Visualization	Figure 5.1

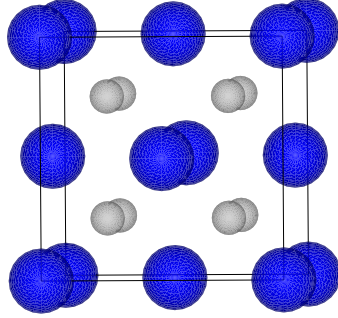


Figure 5.1: Li_2O conventional cell in the face-centered cubic structure. The conventional cell lattice constant is 4.53 \AA . The Li atoms are indicated by the smaller gray balls, while the larger blue balls correspond to oxygen atoms.

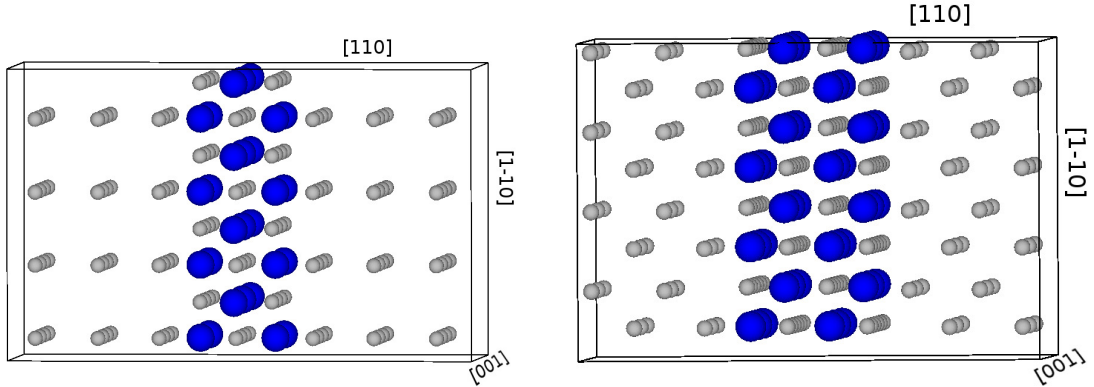
ture. Interestingly, this randomized structure search method resulted in a structure equivalent to a strained fcc Li structure cleaved along its (110) plane. As part of my configuration search, I discovered several variations of this structure with lower symmetry and very similar energies, consistent with the complicated phase diagram of Li.⁴¹

For both configurations I calculated $\tilde{\gamma}_{ab}$, which varies linearly with n_b as predicted by equation 3.6 and shown in Figure 5.3. The calculated values of $\tilde{\gamma}_{ab}^{lim}$ are 30 meV/\AA^2 and 26 meV/\AA^2 for the $\text{Li}_2\text{O}/\text{Li}(\tilde{\Omega}_1)$ and the $\text{Li}_2\text{O}/\text{Li}(\tilde{\Omega}_2)$ configurations respectively, while the associated values of σ are $6.1 \text{ meV/\AA}^2/\text{Li}$ and $0.2 \text{ meV/\AA}^2/\text{Li}$. The large value of $\sigma(\tilde{\Omega}_1)$ is due to the unphysical nature of the orthorhombic Li configuration. The small value of $\sigma(\tilde{\Omega}_2)$ on the other hand suggests that this configuration is close to a preferred equilibrium geometry of Li and that $\tilde{\Omega}_2 \approx \Omega_2$. According to the reasoning outlined in equation 3.7, this implies that for this case, the coherent limit of the interface energy is close to the physical value so that for this interface, $\tilde{\gamma}_{ab}^{lim}(\tilde{\Omega}) \approx \gamma_{ab}(\Omega)$.

The two configurations exhibit markedly different Li structures, both within the Li slab and at the $\text{Li}_2\text{O}/\text{Li}$ interface. The similarity in their interface energies in spite of their dissimilar structures suggests that multiple interface configurations may exist near this value of the interface energy.

5.2 Interface partial density of states

In addition to the interface geometries and interface energies, the partial density of states provide insight into the nature of the atomic interactions at the interface. I calculated the atom decomposed partial density of states $N^a(E)$ for bulk Li, bulk Li_2O , and for the $\text{Li}_2\text{O}/\text{Li}(\tilde{\Omega}_1)$ and the $\text{Li}_2\text{O}/\text{Li}(\tilde{\Omega}_2)$ configurations. The atoms are



(a) $\text{Li}_2\text{O}/\text{Li}(\tilde{\Omega}_1)$ configuration showing the interface between the (110) face of Li_2O and an orthorhombic Li structure derived from the Li structure within Li_2O .

(b) $\text{Li}_2\text{O}/\text{Li}(\tilde{\Omega}_2)$ configuration showing the interface between the (110) face of Li_2O and a Li structure similar to bulk Li under strain. The strained Li exhibits bond lengths characteristic of multiple Li phases.

Figure 5.2: $\text{Li}_2\text{O}/\text{Li}$ interfaces in the sandwich configuration for two different Li structures. In 5.2a the Li_2O is cleaved along the 110 face and the Li structure in subfigure a is based on the Li structure in Li_2O , while the Li in subfigure b was generated from randomized Li positions and resembles the structure of bulk Li under strain. In both cases the number of layers of Li_2O was adjusted so that within a given simulation the interfaces on both sides of the simulation cell were equivalent.

grouped into sets on the basis of the similarity of their atomic density of states as described in equation 4.1. These results are depicted in Figure 5.4.

As shown in Figure 5.4c, for the $\text{Li}_2\text{O}/\text{Li}(\tilde{\Omega}_1)$ interface $N^s(E)$ for the Li_2O is relatively similar to the bulk density shown in Figure 5.4a. The metallic Li states on the other hand differ significantly from the bulk $N^s(E)$ given in Figure 5.4b. The bottom of the Li (slab) bands are near the top of the Li_2O valence bands and the Fermi level of the system is 0.8 eV higher than in the bulk like Li structure shown in Figure 5.4b. The density associated with the Li in the first layer of the metallic slab exhibit both Li_2O -like and Li slab-like character in the corresponding energy ranges.

As shown in Figure 5.4d, for the $\text{Li}_2\text{O}/\text{Li}(\tilde{\Omega}_2)$ interface, the Li_2O $N^s(E)$ is also relatively unchanged from that of bulk Li_2O . Consistent with my earlier identification of the Li slab as bulk-like for this configuration, I observe that the states within the Li slab are very similar to those for bulk Li shown in Figure 5.4a, while $N^s(E)$ for the Li at the interface exhibits a mixture of Li_2O -like and Li-like states. The observation that the states are relatively unchanged from the bulk outside of the first layer of Li is in good agreement with my results from the previous section which showed that the difference in interface energy between systems with multiple layers of Li could be attributed to lattice strain and not to interactions at the interface.

For both cases the relatively small modifications relative to the bulk density of states agrees well with the observed stability of these interfaces.

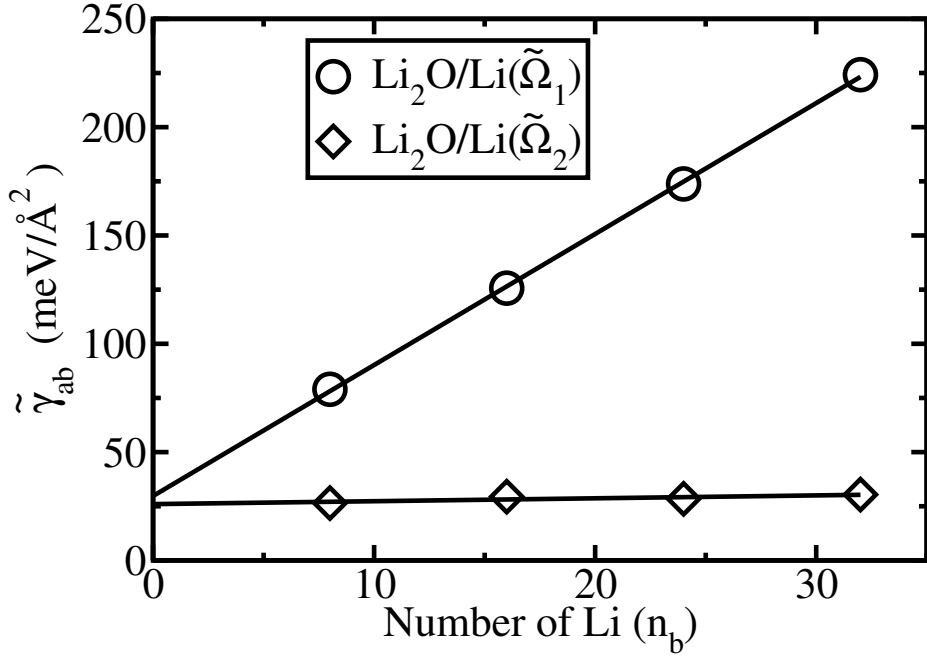
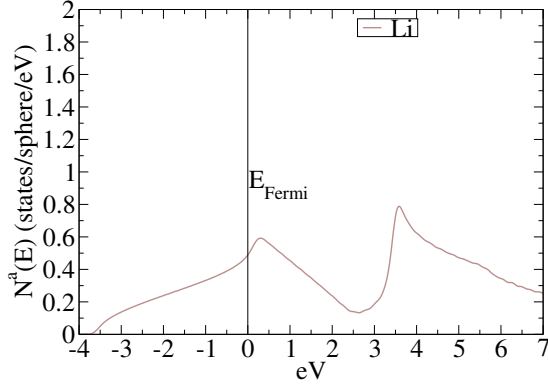
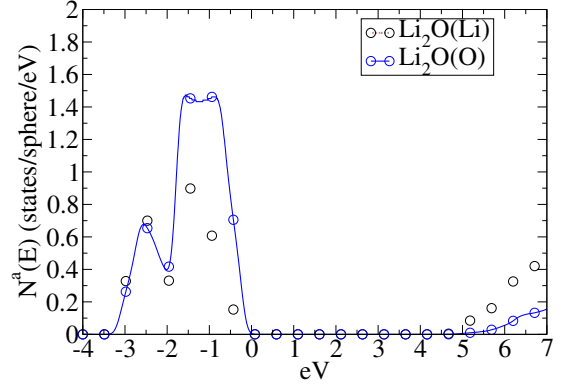


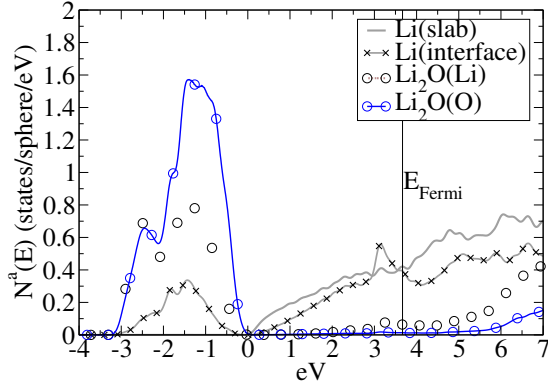
Figure 5.3: Plot of $\tilde{\gamma}_{ab}$ for the Li₂O/Li($\tilde{\Omega}_1$) and the Li₂O/Li($\tilde{\Omega}_2$) interfaces showing the linear variation described in equation 3.6. The y-intercept of the graph corresponds to $\tilde{\gamma}_{ab}^{lim}$ and has the value 0.030 eV/Å² for the Li₂O/Li($\tilde{\Omega}_1$) configuration and 0.026 for the Li₂O/Li($\tilde{\Omega}_2$) configuration. The slope of the fit lines for the two configurations is 6.05 meV/Å²/Li for the Li₂O/Li($\tilde{\Omega}_1$) configuration and 0.225 meV/Å²/Li for the Li₂O/Li($\tilde{\Omega}_2$) configuration. These values are summarized in Table 9.1 on page 47.



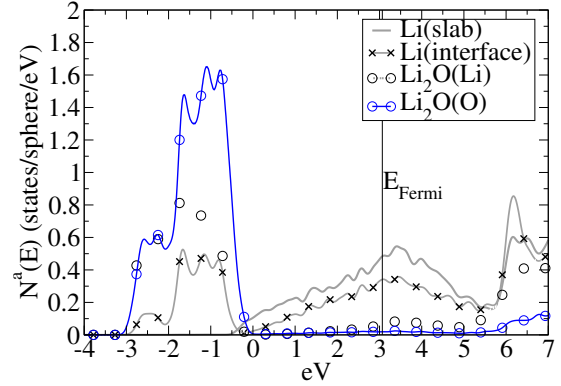
(a) Density of states for Li metal in the bcc structure.



(b) Atom decomposed partial density of states for Li_2O in the $\text{Fm}\bar{3}\text{m}$ structure.



(c) $\text{Li}_2\text{O}/\text{Li}(\tilde{\Omega}_1)$ configuration partial density of states separated out to show the density associated with the Li and oxygen within Li_2O , the density associated with the first layer of metallic Li at the interface, and the density associated with the interior of the Li slab. The geometry of this configuration is depicted in Figure 5.2a.



(d) $\text{Li}_2\text{O}/\text{Li}(\tilde{\Omega}_2)$ configuration partial density of states separated out to show the density associated with the Li and oxygen within Li_2O , the density associated with the first layer of metallic Li at the interface, and the density associated with the interior of the Li slab. The geometry of this configuration is depicted in Figure 5.2b. The states associated with the Li slab closely resemble those associated with bcc Li.

Figure 5.4: Figures showing the atom decomposed partial density of states for bulk Li, bulk Li_2O , and two $\text{Li}_2\text{O}/\text{Li}$ interface configurations. $N^s(E)$ is determined in accordance with equation 4.1, and the scale of the Li atomic density has been increased by a factor of ten for the sake of visibility. The Li at the electrolyte/metal interface appears to have both metal-like and electrolyte-like states.

Chapter 6

Li₂S/Li System

6.1 Li₂S/Li interfaces

I investigated the interface between Li₂S and metallic Li. While crystalline Li₂S is not, by itself, a likely electrolyte material, it has been used as a cathode material in Li-S batteries,⁵¹ and sulfide glass electrolyte containing Li₂S-P₂S₅ mixtures are an area of active research.⁵² Additionally, my previous work suggests that Li₂S may play an important role at Li metal interfaces in other thiophosphate electrolyte materials.³¹

I considered multiple possible interfaces between Li₂S and Li metal, and four representative cases are depicted in Figure 6.2. The calculated lattice constant for Li₂S (*Fm* $\bar{3}$ *m*) was 5.57 Å. The supercells used to model the interfaces were orthorhombic, and in the interface plane the cell dimensions were 5.57 Å in the $\langle 100 \rangle$ directions and 7.88 Å in the $\langle 110 \rangle$ directions. The cell dimension orthogonal to the interface varied depending on the number of electrolyte layers and Li atoms. In each case the number of electrolyte layers was adjusted so that the interfaces on both sides of the simulation cell were symmetric.

The $\tilde{\Omega}_1$ and $\tilde{\Omega}_2$ configurations shown in Figure 6.2(b) and (a) are comprised of Li₂S cleaved along a (110) plane combined with an orthorhombic Li structure based on the Li placements in Li₂S. The extrapolated interface energy for Li₂S/Li($\tilde{\Omega}_1$) is $\tilde{\gamma}_{ab}^{lim} = 47$ meV/Å² while the slope of the fit line is $\sigma = 4$ meV/Å²/Li. For Li₂S/Li($\tilde{\Omega}_2$) the interface energy is $\tilde{\gamma}_{ab}^{lim} = 11$ meV/Å² while the slope of the fit line is also $\sigma = 4$ meV/Å²/Li. While both configurations are based on similar Li and Li₂S geometries, they differ in the relative alignment of the two materials at the interface. This is reflected in the similarity of $\sigma(\tilde{\Omega}_1)$ and $\sigma(\tilde{\Omega}_2)$ as well as the appreciable difference between $\tilde{\gamma}_{ab}^{lim}(\tilde{\Omega}_1)$ and $\tilde{\gamma}_{ab}^{lim}(\tilde{\Omega}_2)$.

The third configuration, Li₂S/Li($\tilde{\Omega}_3$), shown in Figure 6.2(c) is the interface between the (110) face of Li₂S and a Li configuration generated by allowing sets of randomized initial Li positions to relax. As in the Li₂S/Li($\tilde{\Omega}_2$) configuration, the Li positions in the Li metal at the interface closely resemble the positions of Li atoms in Li₂S. The Li₂S/Li($\tilde{\Omega}_3$) configuration is not closely related to any readily identifiable Li structure but its density is comparable to the fcc and bcc phases of bulk Li. The extrapolated interface energy is $\tilde{\gamma}_{ab}^{lim} = 19$ meV/Å², and the slope of the fit line is

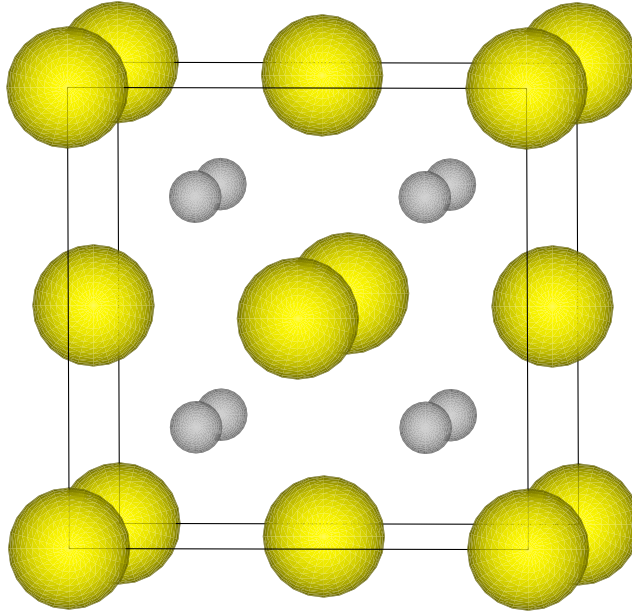


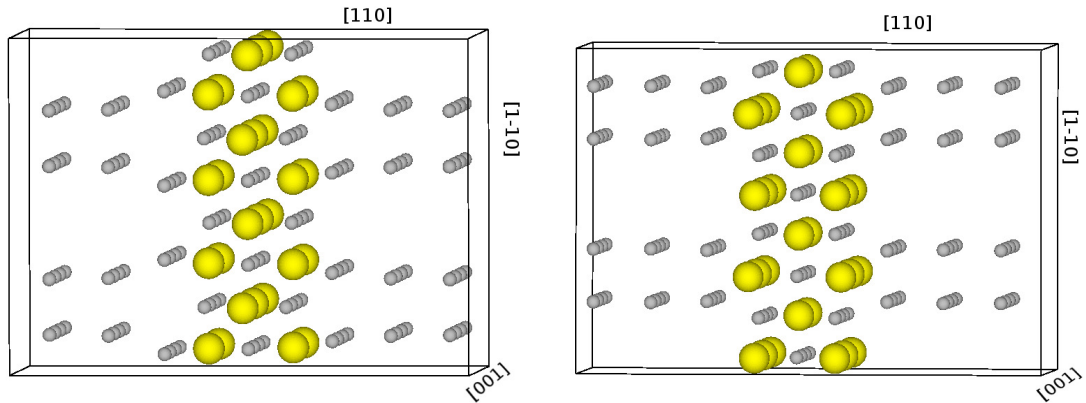
Figure 6.1: Li_2S conventional cell in the face-centered cubic structure. The conventional cell lattice constant is 5.57 \AA . The Li atoms are indicated by the smaller gray balls, while the larger yellow balls correspond to sulfur atoms.

$$\sigma = 0.2 \text{ meV}/\text{\AA}^2/\text{Li}.$$

The last of the four cases, shown in Figure 6.2d represents an interface between a Li_2S cleaved along the (100) face and a bulk like Li structure derived from randomized Li positions. Stoichiometric Li_2S cleaved in the [100] direction results in a polar surface. It does not have identical interfaces at both sides of the Li_2S slab, but is instead Li terminated on one side of the slab and S termination on the other. However, when placed in contact with Li metal, the first layer of the Li metal at the S terminated side of the slab relaxes to a configuration identical to that observed on the Li terminated side of the slab and the resulting configurations on both sides of slab are equivalent. The extrapolated interface energy for the $\text{Li}_2\text{S}/\text{Li}(\tilde{\Omega}_4)$ interface configuration is $\tilde{\gamma}_{ab}^{lim} = 19 \text{ meV}/\text{\AA}^2$, and the slope of the fit line is $\sigma = 0.0 \text{ meV}/\text{\AA}^2/\text{Li}$.

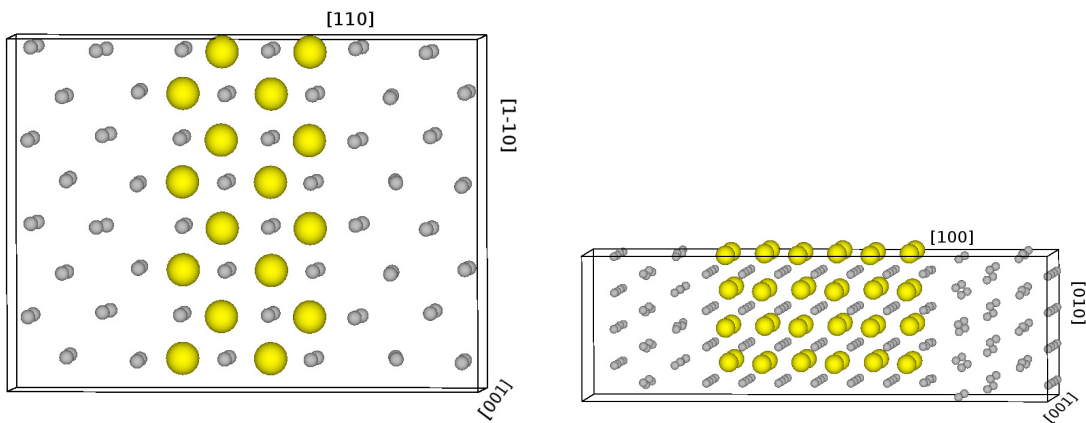
In principle the Li at the interface in several of these examples, especially the $\text{Li}_2\text{S}/\text{Li}(\tilde{\Omega}_4)$ configuration could be identified as belonging to either the Li_2S or metallic Li. Because γ_{ab} depends on the amount of each material, this ambiguity could have implications for the interface energy, since equivalent interface systems could be constructed from non-stoichiometric slabs with lithium or sulfur terminations on both sides. I have restricted my analysis to the stoichiometric case.

Interestingly, the calculated interface energy for the $\text{Li}_2\text{S}[110]$ surface and the $\text{Li}_2\text{S}[100]$ surface are very similar. This suggests that the surface energy may not depend strongly on the cleavage of the Li_2S for this system if the Li metal is not constrained. Experimental work on liquid metal/solid insulator interfaces has also observed that the interface energy does not always depend strongly on the exposed cleave of the solid.⁵³



(a) $\text{Li}_2\text{S}/\text{Li}(\tilde{\Omega}_1)$ configuration showing the interface between the (110) face of Li_2S and a Li configuration derived from the Li positions in Li_2S .

(b) $\text{Li}_2\text{S}/\text{Li}(\tilde{\Omega}_2)$ configuration showing the interface between the (110) face of Li_2S and a Li configuration derived from the Li_2S Li configuration, but shifted so that the Li do not attempt to line up over the S atoms at the surface.



(c) $\text{Li}_2\text{S}/\text{Li}(\tilde{\Omega}_3)$ configuration showing the interface between the (110) face of Li_2S and a Li structure based on optimizing randomly generated Li positions.

(d) $\text{Li}_2\text{S}/\text{Li}(\tilde{\Omega}_4)$ configuration showing the interface between the (100) face of Li_2S and a Li structure based on optimizing randomly generated Li positions.

Figure 6.2: Figures depicting the $\text{Li}_2\text{S}/\text{Li}$ interface in the sandwich configuration for two different Li_2S cleavages and 3 different Li structures. The Li_2S is cleaved along both the 100 and the 110 face and the Li structure in subfigures a and b is based on bulk Li under strain, while the Li structure in subfigures c and d is based on the Li structure within the Li_2S . In all cases the number of layers of Li_2S was adjusted so that within a given simulation the interfaces on both sides of the sandwich were equivalent.

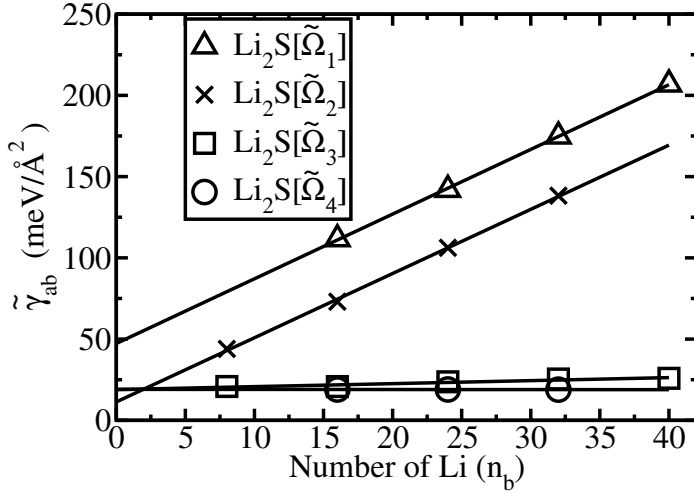


Figure 6.3: Plot of $\tilde{\gamma}_{ab}$ for the $\text{Li}_2\text{S}/\text{Li}(\tilde{\Omega}_i)$ interfaces for $i = 1-4$ showing the linear relationship described in equation 3.6. The numerical values are summarized in Table 9.1.

6.2 Interface partial density of states

The partial densities of states of the Li_2/Li interfaces are shown in Figure 6.5. For all four of the interface configurations, the contributions from the occupied states of Li_2S are similar to those of the bulk shown in Figure 6.4a. There is some variation in the $N^s(E)$ curves in Figure 6.5 due to varying degrees of under-coordination of the S atoms at the interfaces.

In particular, for the $\tilde{\Omega}_1$ structure shown in Figure 6.5a, the upper peak can be attributed to the under-coordinated interface S site seen in Figure 6.2b. For configurations $\tilde{\Omega}_1$, $\tilde{\Omega}_2$, and $\tilde{\Omega}_3$, the Fermi level appears to lie within the conduction band of Li_2S . A more detailed analysis shows that these contributions are confined to the surface layer of the Li_2S slab; the bulk layers have no appreciable occupancy of the conduction band states.

$N^s(E)$ for configurations $\tilde{\Omega}_1$ (a) and $\tilde{\Omega}_2$ (b) represent highly strained models of the Li slabs and the corresponding Li(slab) contributions differ significantly from that of bulk Li shown in Figure 6.4b. Configurations $\tilde{\Omega}_3$ (c) and $\tilde{\Omega}_4$ (d) have Li slabs that are closer to the bulk geometry and the corresponding curves are similar to that of bulk Li (apart from k-point sampling errors). Interestingly, for both of these configurations, the Li (slab) contribution begins approximately -1 eV below the top of the valence band of Li_2S . It is also interesting to note that the configuration $\tilde{\Omega}_4$ formed from the polar [100] surface of Li_2S , in this sandwich geometry behaves very similarly to the configuration $\tilde{\Omega}_3$ which was formed from the non polar [110] surface.

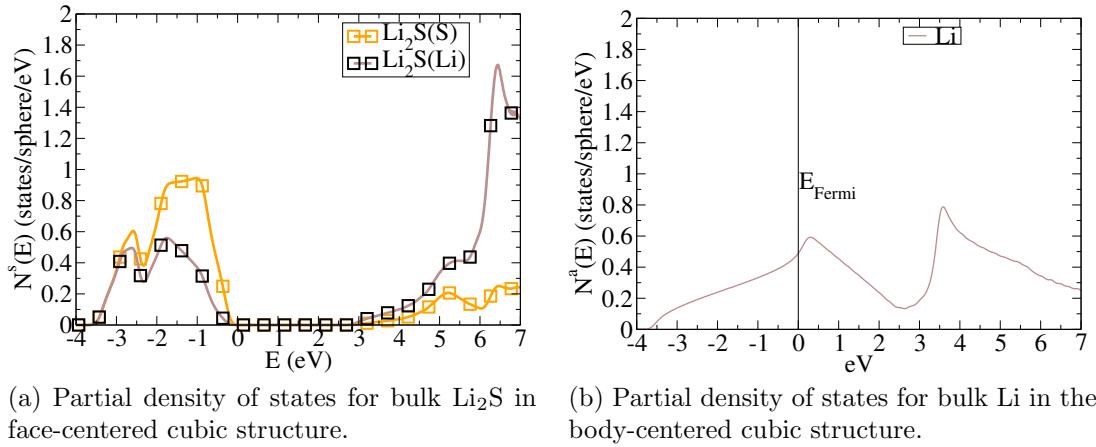


Figure 6.4: Partial density of states for bulk Li_2S and Li metal in the bcc structure. The Li density shown here is identical to that in figure 5.4.

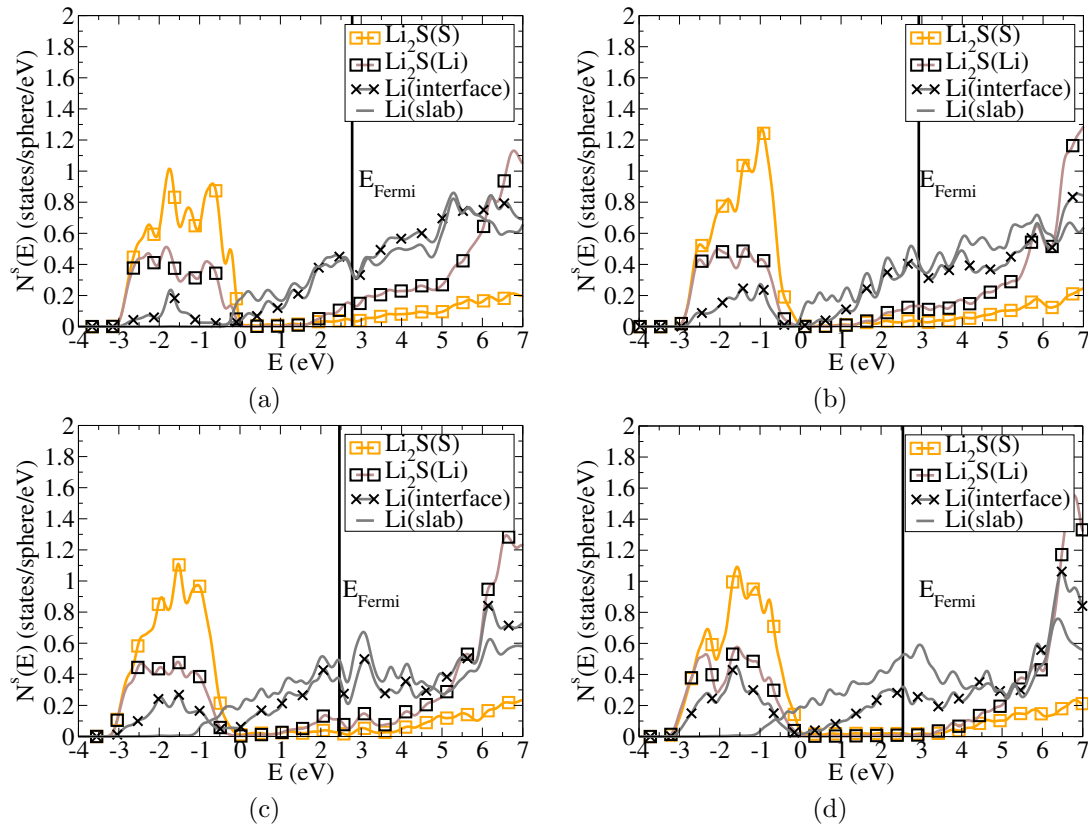


Figure 6.5: Partial densities of states for the $\text{Li}_2\text{S}/\text{Li}$ interfaces for the (a) $\tilde{\Omega}_1$, (b) $\tilde{\Omega}_2$, (c) $\tilde{\Omega}_3$, and (d) $\tilde{\Omega}_4$ configurations.

Chapter 7

Li₃PO₄/Li System

Li₃PO₄ is a potential solid electrolyte that has garnered significant interest in part because of its close relationship to the commercial solid electrolyte LiPON. The ionic conductivities of Li₃PO₄ and the various LiPON materials are too low for them to serve as a bulk electrolytes in traditionally manufactured power batteries. Li₃PO₄-like materials have been used in thin film batteries, and as a passivating coating at Li-ion battery interfaces. The interest in Li₃PO₄ as a solid electrolyte material is due to its excellent electrochemical stability.

Li₃PO₄ exists in multiple crystal forms, but battery research has primarily focused on the β -Li₃PO₄ and γ -Li₃PO₄ materials. These two materials have very similar structures. Both form orthorhombic crystals comprised of Li atoms and PO₄ tetrahedra. β -Li₃PO₄ crystallizes in the Pmn2₁ structure while γ -Li₃PO₄ forms the Pnma structure. The two structures are related by a rotation, so that the **a** axis in the β -Li₃PO₄ material corresponds to the **b** axis in the γ -Li₃PO₄ material while the **a** axis in the γ -Li₃PO₄ material corresponds to twice the **b** axis in the β -Li₃PO₄ structure.

Table 7.1: Li₃PO₄ Data Table

β -Li ₃ PO ₄	Symmetry	Pmn2 ₁ (#31)
	Calc. Lattice (Å)	6.00, 5.13, 4.74
	Formula Units/Cell	2
	Formation Enthalpy	-21.31 eV
γ -Li ₃ PO ₄	Symmetry	Pnma (#62)
	Calc. Lattice (Å)	10.28, 5.99, 4.82
	Formula Units/Cell	4
	Formation Enthalpy	-21.28 eV

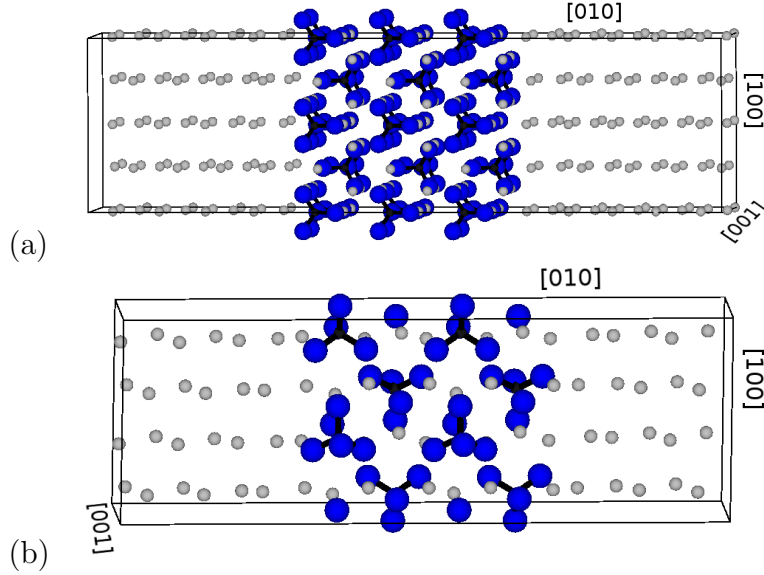


Figure 7.1: Structural diagrams of supercells for $\text{Li}_3\text{PO}_4/\text{Li}$ interfaces with Li, P, and O atoms represented by small gray, tiny black, and medium blue balls respectively. (a) $\text{Li}_3\text{PO}_4/\text{Li}(\tilde{\Omega}_1)$ interface of $[010]$ $\beta\text{-Li}_3\text{PO}_4$ and a Li slab. (b) $\text{Li}_3\text{PO}_4/\text{Li}(\tilde{\Omega}_3)$ interface of $[010]$ $\gamma\text{-Li}_3\text{PO}_4$ and a Li slab.

7.1 $\text{Li}_3\text{PO}_4/\text{Li}$ interfaces

As part of my investigation of Li_3PO_4 I evaluated the surface energy of multiple Li_3PO_4 surfaces, including both the $\beta\text{-Li}_3\text{PO}_4$ (010) surface plane and the $\gamma\text{-Li}_3\text{PO}_4$ (100) and (010) surface planes. These surfaces were chosen because they are defined by planes perpendicular to the lattice planes that do not disrupt the PO_4 tetrahedra. Surfaces with broken PO_4 tetrahedra, or with additional tetrahedra protruding from the surface exhibit higher surface energies than the chosen surfaces.

The surface energy of the $\beta\text{-Li}_3\text{PO}_4$ (010) surface is $39 \text{ meV}/\text{\AA}^2$. The surface energies for the $\gamma\text{-Li}_3\text{PO}_4$ (100) and (010) surfaces are $40 \text{ meV}/\text{\AA}^2$ and $73 \text{ meV}/\text{\AA}^2$ respectively. Because the lattices of the two structures are related by a rotation, the $\beta\text{-Li}_3\text{PO}_4$ (010) surface most closely resembles the $\gamma\text{-Li}_3\text{PO}_4$ (100) surface, and the calculated surface energies are consistent with this geometric similarity.

I constructed Li interfaces for all three systems, and the resulting configurations are labelled with $\tilde{\Omega}_{1-3}$ in keeping with my previous notation. The $\beta\text{-Li}_3\text{PO}_4/\text{Li}(\tilde{\Omega}_1)$ interface between the $\beta\text{-Li}_3\text{PO}_4$ (010) surface and 36 Li atoms, as well as the $\gamma\text{-Li}_3\text{PO}_4/\text{Li}(\tilde{\Omega}_3)$ interface between the $\gamma\text{-Li}_3\text{PO}_4$ (010) surface and 48 Li atoms are both depicted in Figure 7.1.

For all three configurations I calculated $\tilde{\gamma}_{ab}$ following the methodology outlined in the formalism, and these results are shown in Figure 7.2. The close similarity between the (100) plane of $\gamma\text{-Li}_3\text{PO}_4$ and the (010) plane of $\beta\text{-Li}_3\text{PO}_4$ is evident in the close agreement of the $\tilde{\gamma}_{ab}$ values for these interfaces.

As an additional verification of my method I also calculated the interface energy $\tilde{\gamma}_{ab}^{lim}$ for the $\beta\text{-Li}_3\text{PO}_4(\tilde{\Omega}_1)$ configuration depicted in Figure 7.1a using a variation on

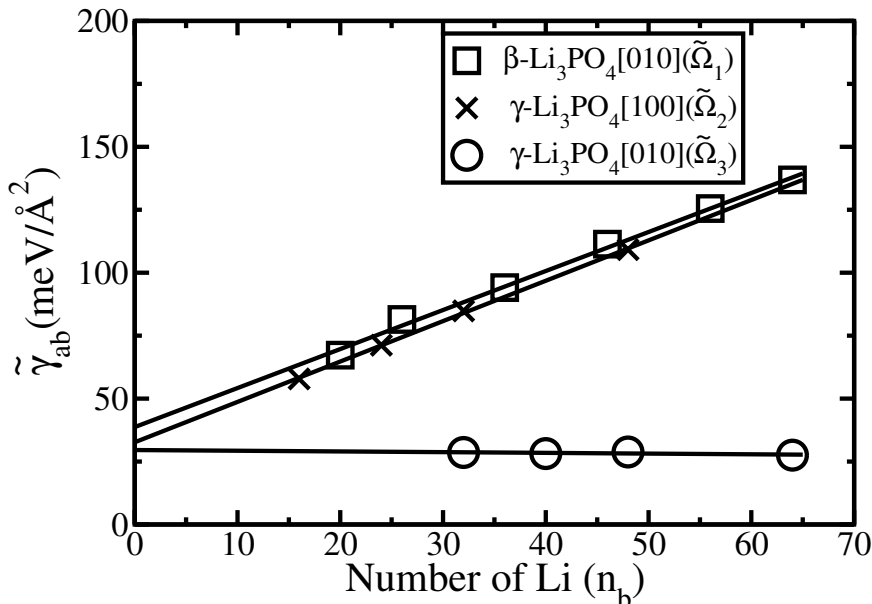


Figure 7.2: Plot of $\tilde{\gamma}_{ab}$ for the $\text{Li}_3\text{PO}_4/\text{Li}(\tilde{\Omega}_i)$ interfaces for $i = 1-3$ showing the linear relationship described in equation 3.6. The numerical values are summarized in Table 9.1 on page 47.

the method outlined in equation 3.6. In this alternative method, the lattice constants of the orthorhombic interface cell were allowed to relax while the angles were held constant. The lattice strain energy in this method was calculated explicitly, by calculating the total energies for both the Li_3PO_4 and Li slabs in the strained configuration and comparing those energies to the corresponding values for slabs simulated using the bulk lattice constants. The interface energy estimated via this alternative method was $41 \text{ meV}/\text{\AA}^2$, in good agreement with the value of $39 \text{ meV}/\text{\AA}^2$ arrived at via the extrapolation method.

7.2 Interface partial density of states

In the partial densities of states for the $\beta\text{-Li}_3\text{PO}_4/\text{Li}$ interface shown in Figure 7.3, the Li_3PO_4 states are even less affected by the presence of Li metal than the electrolyte states in the $\text{Li}_2\text{O}/\text{Li}$ and $\text{Li}_2\text{S}/\text{Li}$ interfaces. The top of the Li_3PO_4 valence band is below the bottom of the metallic Li band. As in the cases of Li_2O and Li_2S interfaces, there is a small amount of occupied electrolyte conduction states just at the interface.

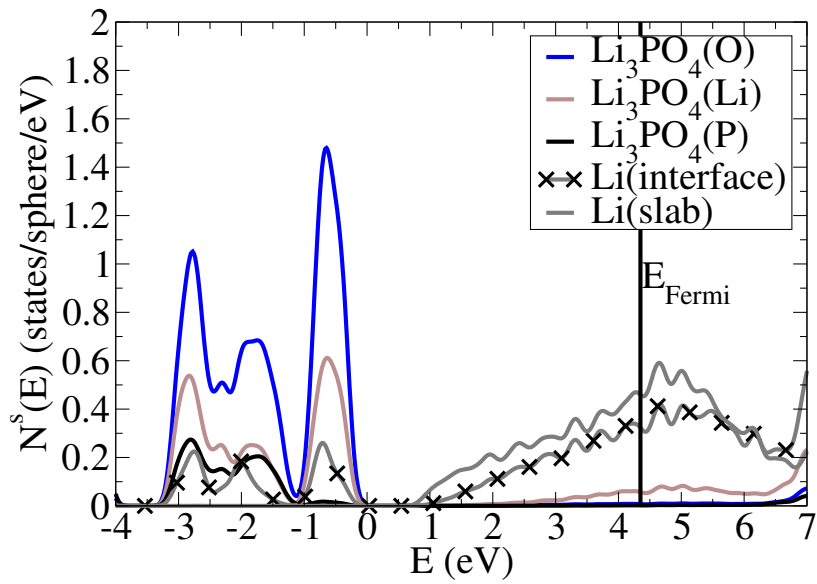


Figure 7.3: Partial density of states for $\text{Li}_3\text{PO}_4/\text{Li}$ interface in the $\tilde{\Omega}_1$ configuration.

Chapter 8

Li₃PS₄ Interfaces

Li₃PS₄ is a potential solid electrolyte material that has been the subject of considerable interest. While the ionic conductivity of bulk Li₃PS₄ itself has only been measured to be around $2.63\text{--}8.93 \times 10^{-4}$ mS/cm, the conductivity of closely related compounds such as Li₇P₃S₁₁ and the Li₁₀GePS₁₂ family of materials have been observed in the 0.1–12 mS/cm range, competitive with the room temperature conductivity of existing liquid electrolytes (10 mS/cm).⁵⁴ These high-conductivity phases are in general somewhat unstable with respect to Li₃PS₄ in the sense that

$$\Delta H(\text{Li}_7\text{P}_3\text{S}_{11}) \longrightarrow \Delta H(\text{Li}_3\text{PS}_4) + \Delta H(\text{Li}_4\text{P}_2\text{S}_6) + 0.78 \text{ eV} . \quad (8.1)$$

The metastability of these highly conducting phases means that they may not be robust enough for commercial battery applications. At the same time, the existence of several highly conducting material phases closely related to Li₃PS₄ underscores the potential of the Li₃PS₄ system. In addition to the bulk crystalline structures mentioned previously, there have been attempts to study more highly conducting glassy and nanostructured forms of Li₃PS₄.⁵⁵

Table 8.1: Li₃PS₄ Data Table

γ -Li ₃ PS ₄	Symmetry	Pmn2 ₁ (#31)
	Calc. Lattice (Å)	7.55, 6.45, 6.05
	Formula Units/Cell	2
	Formation Enthalpy	−8.36 eV
β -Li ₃ PS ₄	Symmetry	Pnma (#62)
	Calc. Lattice (Å)	12.89, 7.80, 5.92
	Formula Units/Cell	4
	Formation Enthalpy	−8.16 eV

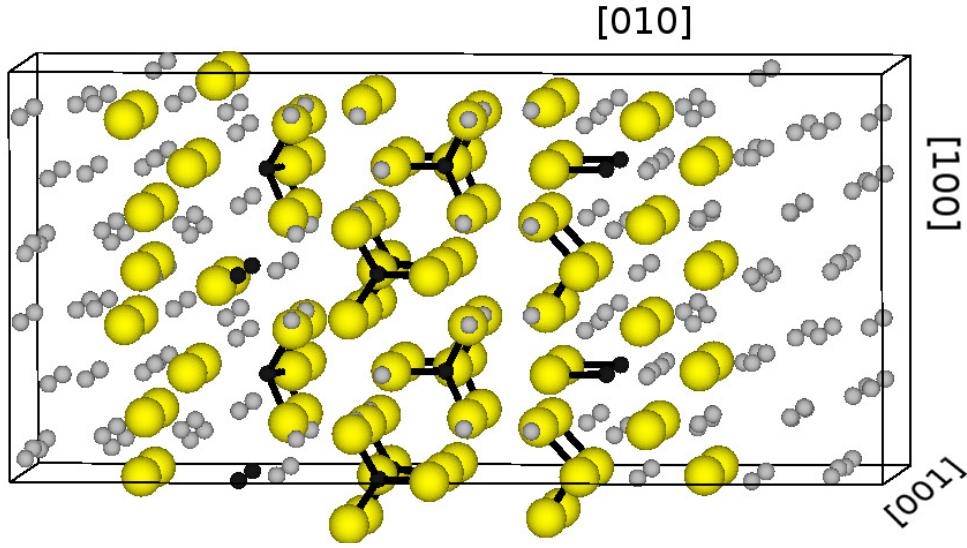


Figure 8.1: Structural diagram of γ -Li₃PS₄[010]/Li interface with 24 Li with Li, P, and S represented by small gray, tiny black, and medium yellow balls respectively.

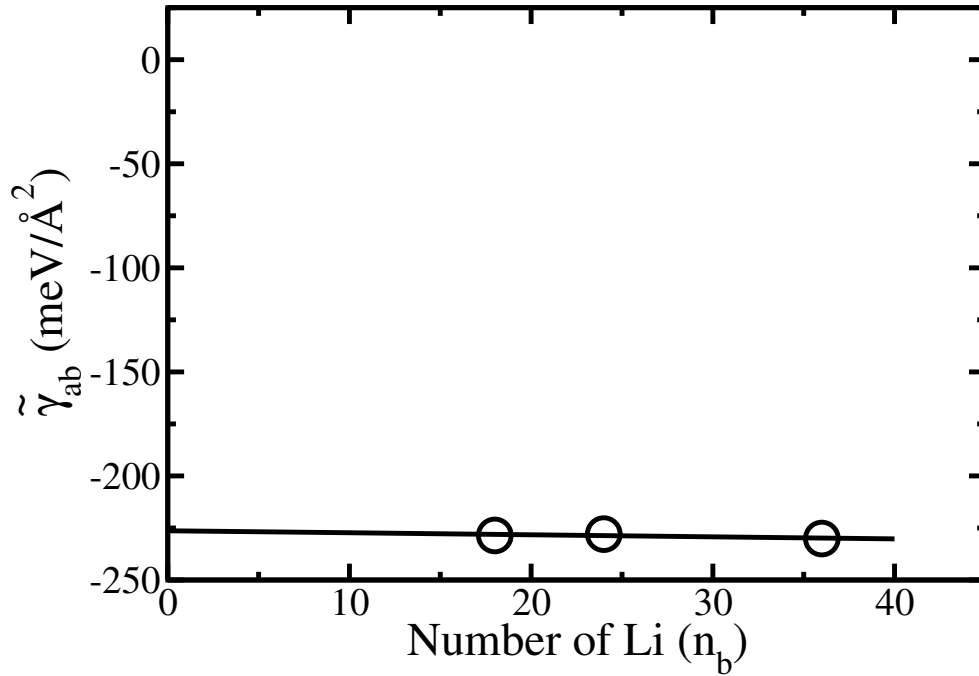


Figure 8.2: Interface energy for the γ -Li₃PS₄[010]/Li interface. The large negative value of $\tilde{\gamma}_{ab}$ is due to chemical reactions that occur at the interface. The bond breaking and bond formation at the interface dominates lattice strain effects.

8.1 $\text{Li}_3\text{PS}_4/\text{Li}$

The interface between Li_3PS_4 and metallic Li exhibits substantial disruption of the Li_3PS_4 structure at the interface as shown in previous work.³¹ While Li_3PS_4 exists in both $\beta\text{-Li}_3\text{PS}_4$ ($Pnma$) and $\gamma\text{-Li}_3\text{PS}_4$ ($Pmn2_1$) phases, the structural and energetic differences between the phases are small compared to the disruption of the electrolyte/anode surface due to Li metal. Consequently, I present quantitative results only for the $\gamma\text{-Li}_3\text{PS}_4$ (010) surface, although my results for the other phases and surfaces are similar.

This interface is visualized in Figure 8.1. The PS_4 tetrahedra near the surface of Li_3PS_4 break apart and bond to the metallic Li, forming a Li_2S -like phase at the interface. This agrees well with experimental results that show the formation of a similar layer at the $\text{Li}/\text{Li}_3\text{PS}_4$ interface.⁵⁶ The disordered nature of the $\text{Li}_3\text{PS}_4/\text{Li}$ interface evident in Figure 8.1 increases the variance in possible interface configurations. The interface energy calculated according to equation 3.6 was $-216 \text{ meV}/\text{\AA}^2$, as shown in Figure 8.2. The large energies associated with the different chemically altered interfaces dominate the energy contributions from the lattice strain.

Observed values for $\tilde{\gamma}_{ab}$ varied between -175 and $-225 \text{ meV}/\text{\AA}^2$, with the variation due primarily to the extent of the decomposition reaction at the interface. For all of the configurations considered, the $\text{Li}_3\text{PS}_4/\text{Li}$ reaction resulted in the formation of a disordered Li_2S -like phase, which appeared to passivate the electrolyte against further degradation. Our zero temperature simulations are expected to underestimate the size of such a passivating layer, and it is not clear from our results alone how robust this insulating layer is. The formation of an electrically insulating layer comprised of amorphous Li_2S and Li_3P could explain the successful use of Li_3PS_4 electrolytes in experiments.

8.2 $\text{Li}_3\text{PS}_4/\text{Li}$ partial density of states

The partial density of states for a $\gamma\text{-Li}_3\text{PS}_4/\text{Li}$ interface is shown in Figure 8.3 with separate panels for the three main regions. The Li slab PDOS in the top panel closely resembles the $N^s(E)$ of bulk Li as shown in Figure 6.4b. Similarly, the $N^s(E)$ for the electrolyte region shown in the bottom panel resembles that of bulk $\gamma\text{-Li}_3\text{PS}_4$ shown in Figure 8.3. The bottom of the Li slab band lies 1.5 eV below the top of the valence band of the electrolyte. The Fermi level for the system, which is determined by the Li slab, lies just below the conduction band of the remaining Li_3PS_4 .

The interface $N^s(E)$ plots are given in the middle panel of Figure 8.3 show the reaction products at the interface. The Li (electrolyte) set refers to Li which interact with P as evidenced by their contributions in the energy range of -7 to -8 eV corresponding to the $3s$ state of P. The Li (interface) contributions refer to the remaining Li atoms in this region and have similar qualitative behavior to the Li (interface) curves for the $\text{Li}_2\text{S}/\text{Li}$ system. The S contributions are divided into “P-S bond” and “no P-S bond” sets, based on their interaction with P, analogous to the Li division.

The close resemblance of the S (no P-S bond) curve to $N^s(E)$ for the $\text{Li}_2\text{S}(\text{S})$

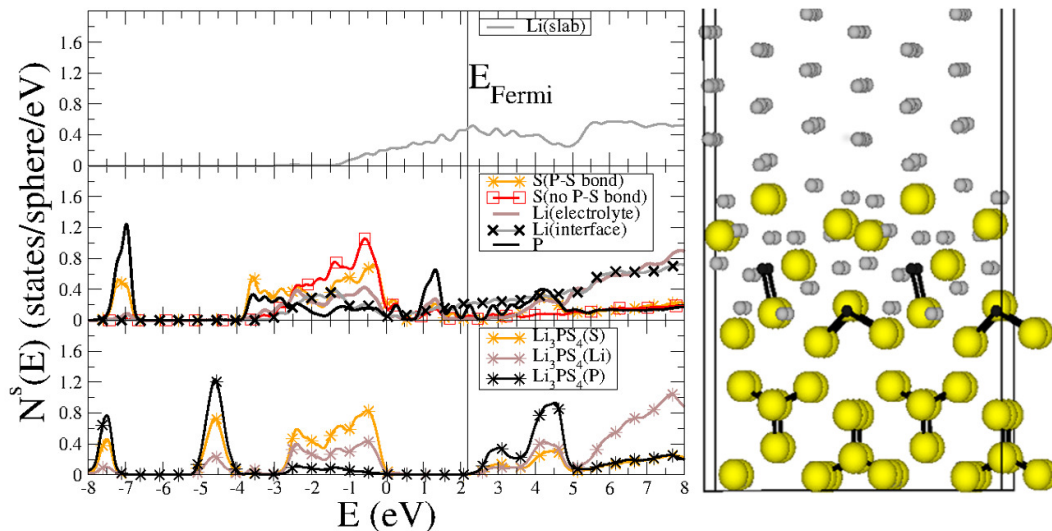


Figure 8.3: Partial density of states for γ - $\text{Li}_3\text{PS}_4/\text{Li}$ interface (left) and corresponding optimized structure (right). The three panels of the $N^s(E)$ plot correspond to the Li slab region, the interface region, and the electrolyte region, respectively.

set shown in Figure 6.5 supports the notion that the reactive layer forms a Li_2S -like phase. Correlated with the formation of Li_2S is the reduction of the P within Li_3PS_4 , which can be seen in the shift of the unoccupied P conduction band states in the bottom panel to occupied states below the system Fermi level in the middle panel.

8.3 $\text{Li}_3\text{PS}_4/\text{Li}_2\text{S}$

Motivated by the formation of an Li_2S -like phase at the $\text{Li}_3\text{PS}_4/\text{Li}$ interface I considered the interface between the γ - Li_3PS_4 (010) and the Li_2S (110) surfaces. The Li_3PS_4 (010) face has lattice constants 6.05 Å and 7.55 Å, while the Li_2S (110) face has lattice constants 5.57 Å and 7.88 Å. The interface was constructed by aligning the dimensions appropriately and straining the Li_2S slab to the γ - Li_3PS_4 lattice. The space groups of the two materials are not compatible with the formation of identical interfaces on both sides of the simulation cell in the sandwich configuration, as can be seen in Figure 8.4.

The estimated interface energy using equation 3.6 is 16 meV/Å² as shown in Figure 8.5. In order to estimate the effect of the asymmetry on the interface energies, I constructed two corresponding sets of vac/ $\text{Li}_3\text{PS}_4/\text{Li}_2\text{S}/\text{vac}$ supercells. The interface energies in these cells were calculated using the same methodology as in the combined system, modified to account for the additional contributions of the vacuum surface energies associated with the Li_2S (110) and Li_3PS_4 (010) surfaces. I found the separate interface energies in these vacuum terminated cells to be 13 meV/Å² and 11 meV/Å². The average of the two separate interface energies is smaller than $\tilde{\gamma}_{ab}$ determined from the sandwich geometry because the interface geometries obtained by relaxing the vac/ $\text{Li}_3\text{PS}_4/\text{Li}_2\text{S}/\text{vac}$ supercells have fewer constraints. The Table 9.1 lists the

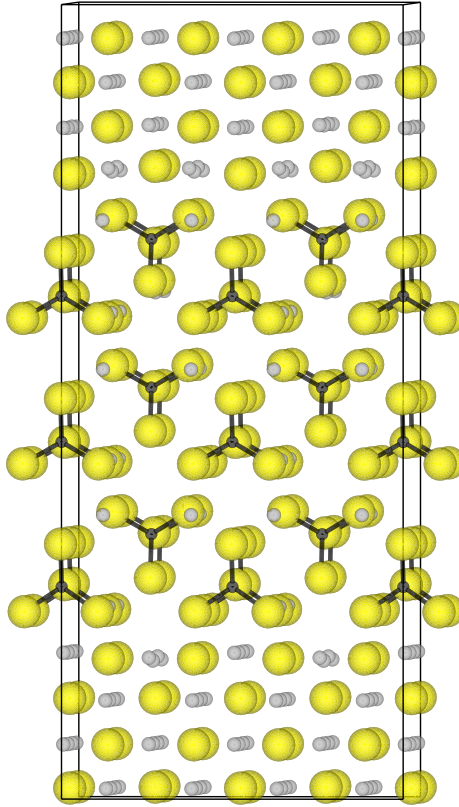


Figure 8.4: Structural diagram of γ - Li_3PS_4 [010]/ Li_2S [110] interface with Li, P, and S represented by small gray, tiny black, and medium yellow balls respectively. The asymmetry of the two interfaces is evident.

value obtained from the sandwich configuration, consistent with the method used for the other materials.

8.4 $\text{Li}_3\text{PS}_4/\text{Li}_2\text{S}$ partial density of states

The partial density of states plot for the $\text{Li}_3\text{PS}_4/\text{Li}_2\text{S}$ interface shown in Figure 8.6 illustrates that two materials are generally not reactive and the S contributions to the occupied states of both materials largely overlap in the energy range of -3.5 – 0 eV. This superposition of the Li_2S valence band and the Li_3PS_4 valence band is also seen in the reactive region of Figure 8.3.

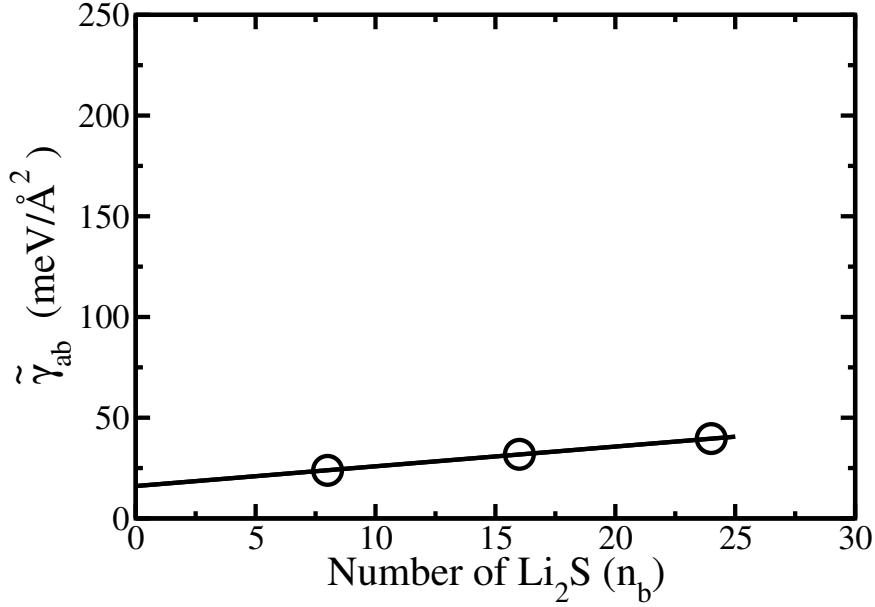


Figure 8.5: Plot of $\tilde{\gamma}_{ab}$ for the γ -Li₃PS₄[010]/Li₂S[110] interface. Numerical values for $\tilde{\gamma}_{ab}^{lim}$ and σ are reported in Table 9.1 on page 47.

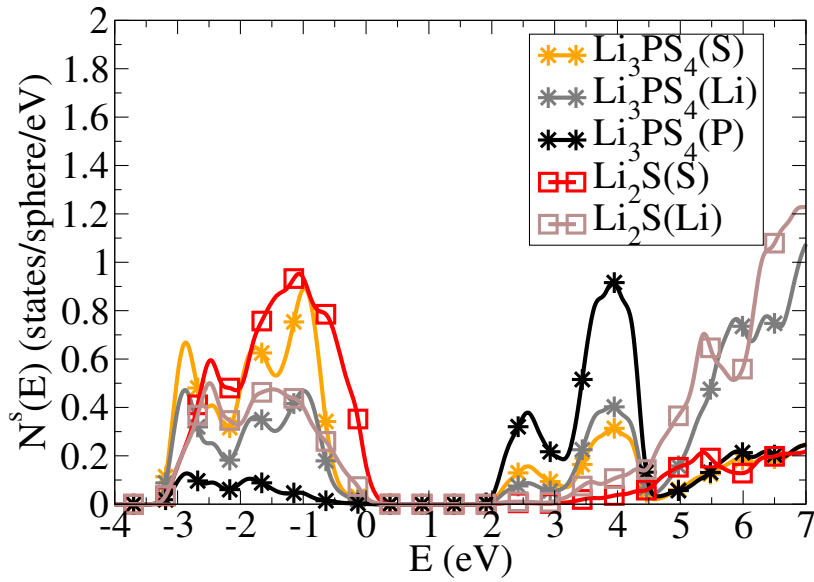


Figure 8.6: Partial density of states for the γ -Li₃PS₄/Li₂S interface. The zero of energy is set to the top of the valence band of γ -Li₃PS₄

Chapter 9

Summary and Conclusions

9.1 Interface energy summary

Table 9.1 summarizes the results for the calculated interface energies; selected surface energies are also included for comparison. The values for $\tilde{\gamma}_{ab}^{lim}$ and σ were determined from a linear fit to equation (3.6). The data was well represented by the linear model, even for small values of n_b , and the estimated error for the non-zero values was on the order of between 1% and 3%. The observation that the linear relationship of equation (3.6) describes the interface energies even for small values of n_b implies that the interface effects are short ranged. The notion that interface interactions are short ranged is also consistent with the observation that $\tilde{\gamma}_{ab}$ is insensitive to the magnitude of n_a .

A review of investigations of Li₂O surface energetics by Hayoun and Meyer⁴³ found that the reported values of the Li₂O [110] surface energy varied between 56 and 90 meV/Å². Our calculated surface energies are consistent with the literature for the non-polar surface of Li₂O,⁴³ Li₂S,^{57,58} and Li₃PO₄.⁵⁹ For modeling the vacuum interfaces I examined the effect of including a self-consistent dipole correction to the structural optimization of the surfaces.⁶⁰ This correction significantly decreased the size of the vacuum region needed to converge the polar Li₂O and Li₂S surfaces, but did not alter the calculated surface energies and structures. The calculated surface energy for the unreconstructed polar surfaces are in excellent agreement with the work of Chen and Kaghazchi.⁵⁷ The calculated surface energies for the unreconstructed polar surfaces of are significantly larger than the non-polar surface energies. This large difference in the surface energies, however, is not observed in the corresponding Li interface systems, where I find that $\tilde{\gamma}_{ab}^{lim}$ for Li₂S[110]/Li($\tilde{\Omega}_3$) is equal to $\tilde{\gamma}_{ab}^{lim}$ for Li₂S[100]/Li($\tilde{\Omega}_4$).

In general, the results of Table 9.1 show that the surface and interface energies of the materials containing oxygen are larger than the values for the corresponding sulfur-containing materials. This trend is consistent with the relatively larger formation energies for the oxide materials compared to those of the corresponding sulfides.

The interface energies have been explicitly shown to be well-converged with respect to system size in the dimension normal to the surface plane. In addition, small values

Table 9.1: Summary of the calculated values of $\tilde{\gamma}_{ab}^{lim}$ in $\text{meV}/\text{\AA}^2$ (*N.B.* $1 \text{ meV}/\text{\AA}^2=16.02 \text{ mJ}/\text{m}^2$.) Also included are the calculated strain energies σ expressed in units of $\text{meV}/\text{\AA}^2/\text{formula unit of material } b$. The final column lists the corresponding structural diagrams.

Configuration ($\tilde{\Omega}$)	$\tilde{\gamma}_{ab}^{lim}$ ($\text{meV}/\text{\AA}^2$)	σ ($\text{meV}/\text{\AA}^2/\text{FU}$)	Visualization
$\text{Li}_2\text{O}[100]/\text{vac}$	304	—	—
$\text{Li}_2\text{O}[110]/\text{vac}$	72	—	—
$\text{Li}_2\text{O}[110]/\text{Li}(\tilde{\Omega}_1)$	30	6.1	Figure 5.2a
$\text{Li}_2\text{O}[110]/\text{Li}(\tilde{\Omega}_2)$	26	0.2	Figure 5.2b
$\text{Li}_2\text{S}[100]/\text{vac}$	162	—	—
$\text{Li}_2\text{S}[110]/\text{vac}$	41	—	—
$\text{Li}_2\text{S}[110]/\text{Li}(\tilde{\Omega}_1)$	47	4.0	Figure 6.2a
$\text{Li}_2\text{S}[110]/\text{Li}(\tilde{\Omega}_2)$	11	4.0	Figure 6.2b
$\text{Li}_2\text{S}[110]/\text{Li}(\tilde{\Omega}_3)$	19	0.2	Figure 6.2c
$\text{Li}_2\text{S}[100]/\text{Li}(\tilde{\Omega}_4)$	19	0.0	Figure 6.2d
$\beta\text{-Li}_3\text{PO}_4[010]/\text{vac}$	39	—	—
$\gamma\text{-Li}_3\text{PO}_4[100]/\text{vac}$	40	—	—
$\gamma\text{-Li}_3\text{PO}_4[010]/\text{vac}$	73	—	—
$\beta\text{-Li}_3\text{PO}_4[010]/\text{Li}(\tilde{\Omega}_1)$	39	1.8	Figure 7.1a
$\gamma\text{-Li}_3\text{PO}_4[100]/\text{Li}(\tilde{\Omega}_2)$	33	1.6	—
$\gamma\text{-Li}_3\text{PO}_4[010]/\text{Li}(\tilde{\Omega}_3)$	31	0.0	Figure 7.1b
$\gamma\text{-Li}_3\text{PS}_4[010]/\text{vac}$	20	—	—
$\gamma\text{-Li}_3\text{PS}_4[010]/\text{Li}$	-216	-0.1	Figure 8.1
$\gamma\text{-Li}_3\text{PS}_4[010]/\text{Li}_2\text{S}[110]$	16	1.0	Figure 8.4

of σ for some of the configurations indicate that these systems are also well converged with respect to system size in the surface plane.

In the course of this study, many interface configurations were considered; these necessarily represent only a small sample of the possible configurations. However, the relatively close agreement among the interface energies $\tilde{\gamma}_{ab}^{lim}$ for the low energy configurations reported here indicates that γ_{ab} is likely to be in this range. Within the results reported in Table 9.1, the interface structures $\tilde{\Omega}$ with small values for both $\tilde{\gamma}_{ab}^{lim}$ and σ are likely to be more representative of the structure of physically realized interfaces.

Direct simulation of the electrolyte/Li and electrolyte/electrolyte interfaces further suggests that all of the interfaces except for that between Li_3PS_4 and metallic Li are at least metastable, while the $\text{Li}_3\text{PS}_4/\text{Li}$ interface is observed to undergo a chemical transformation. This transformation appears to produce a passivating layer with stable $\text{Li}_2\text{S}/\text{Li}$ and $\text{Li}_3\text{PS}_4/\text{Li}_2\text{S}$ interfaces. The greater magnitude of the interface energy associated with the $\text{Li}_3\text{PS}_4/\text{Li}$ interface, relative to that of the other material interfaces is due to the large energies associated with breaking and forming chemical bonds at the interface. The negative sign of the interface energy suggests that the adhesive forces at the interface exceed the cohesive forces holding the respective materials together and is probably a good indicator of a chemically active interface.

9.2 Interface reactions

In addition to describing equilibrium properties of the interface, we also investigated ion transport and chemical reactions involved with the interface. One process that is of particular interest is the migration of metallic Li from the anode into the electrolyte. I studied this phenomenon in the $\text{Li}_3\text{PO}_4/\text{Li}$ system and found that if I removed a Li atom from the Li slab and placed it into a stable interstitial site in the electrolyte as visualized in Figure 9.1, the associated electron remained in the slab. For this system, the fact that the metallic states are well separated from those of the electrolyte allowed us to determine that the number of electrons in the metallic bands was one greater than the number of Li atoms remaining in the slab by counting the states in each energy range.

Quantitative analysis of this effect using supercells and periodic boundary conditions is complicated by the relatively large electric fields associated with the charge separation process. The partial densities of states for the system shown in Figure 9.1 are strongly affected by the electric fields E_1 and E_2 which are due to the separation between the positive charge at the interstitial site and the excess negative charge in the metal slab. The magnitude of these electric fields can be estimated by analyzing the densities of states associated with core electrons of P at different positions within the electrolyte. I found that for this geometry, the electric fields in the interface normal direction (y) have magnitudes of approximately $eE_1 = 0.54 \text{ eV}/\text{\AA}$ and $eE_2 = 0.27 \text{ eV}/\text{\AA}$ in the regions above and below the interstitial site respectively, as indicated in Figure 9.1. In order to separate the intrinsic partial densities of states of this system from the effects of these fields, I adapted the partial densities of states

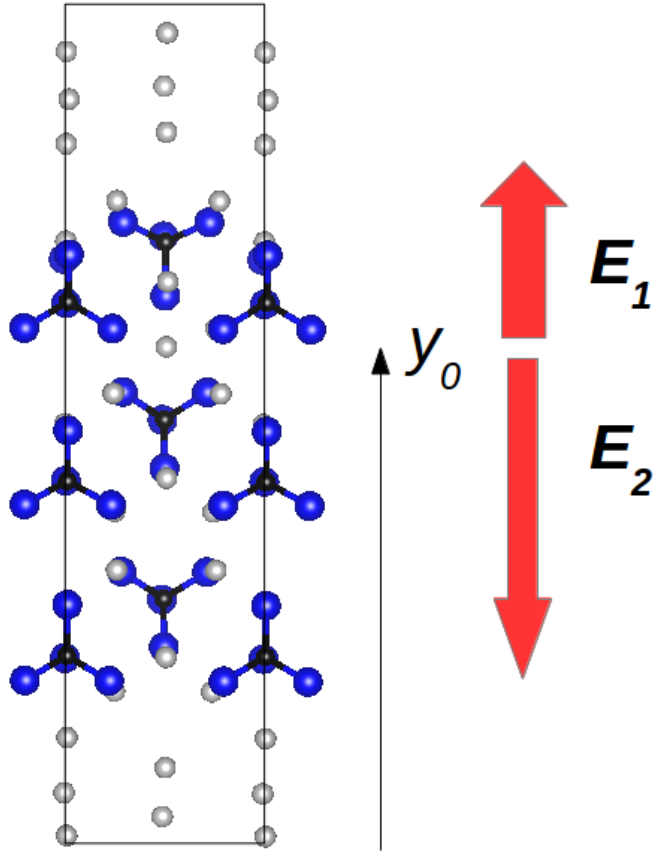


Figure 9.1: Structural diagram of a supercell of $\beta\text{-Li}_3\text{PO}_4[010]/\text{Li}$ with an interstitial defect and 11 Li atoms in the metallic slab. Li, P, and O sites are indicated with small gray, tiny black, and medium blue balls respectively. The vertical direction of the diagram is oriented along the interface normal direction (y). The red arrows indicate the direction, extent (length of arrow) and magnitude (width of arrow) of the electric fields E_1 and E_2 within the electrolyte.

analysis (equation 4.1) as follows. I assumed that the fields are well approximated as occurring only within the electrolyte and vary only in the y direction so that their effects are to shift the local band energy relative to the energy at the location (y_0) of the interstitial Li^+ so that

$$N_{\text{corr}}^s(E) = \frac{1}{M_s} \sum_{a \in s} N^a(\epsilon(E, y_a)) \quad \text{where} \quad (9.1)$$

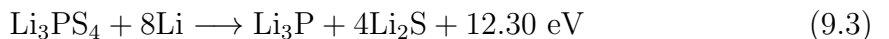
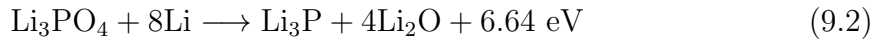
$$\begin{aligned} \epsilon(E, y_a) = E - (y_a - y_0)eE_1\Theta(y_a - y_0) \\ - (y_0 - y_a)eE_2\Theta(y_0 - y_a), \end{aligned}$$

where $\Theta(x)$ denotes the Heaviside step function, eE_1 and eE_2 represent the magnitudes of the estimated electric fields mentioned above, and y_a denotes the position of atom a . The partial density of states associated with the metallic Li slab is unaffected.

$N_{\text{corr}}^s(E)$ for this system is visualized in Figure 9.2, which illustrates the alignment of both the core and valence states throughout the electrolyte. While there remains some distortion of the partial densities of states curves due to the strong electric fields, the general shape and width is similar to that for the interface system without the interstitial Li^+ shown in Figure 7.3, validating the electric field estimates. The interstitial Li^+ site is located only 2 Å from one of the oxygens in Li_3PO_4 . This proximity strongly affects its partial density of states; the corresponding $N_{\text{corr}}^s(E)$ for this unique oxygen and the interstitial Li^+ are plotted separately. $N_{\text{corr}}^s(E)$ for the interstitial Li^+ is confined to the valence energy region of the electrolyte, consistent with its characterization as an ion.

The energy associated with forming the defect configuration shown in Figure 9.1 in my simulation is 2.1 eV, consistent with previous work by Santosh and co-workers.^{59,61} A large component of this energy is due to the electrostatic interaction between the Li^+ and the excess negative charge in the metallic slab. The negative charge remaining in the anode is an appropriate model of a battery in an open circuit where there is no ionic or electronic current flow, consistent with the high calculated energy for Li^+ migration. By contrast, in a discharging battery, the flow of electrons in response to the chemical potential difference between the electrodes results in the anode becoming positively charged. In Li ion battery cells the anode is typically charged to +3 V or more relative to the cathode. Under these conditions we expect the transport of Li^+ ions into the electrolyte to have a substantially reduced or negligible energy barrier.

Another interesting consideration for these systems is their interface stability. In the previous section I showed that it is possible to form stable $\text{Li}_3\text{PO}_4/\text{Li}$ interfaces, while the $\text{Li}_3\text{PS}_4/\text{Li}$ interface decomposes. In spite of this contrast, if one considers the possibility of exposing either Li_3PO_4 or Li_3PS_4 to metallic Li, both of the following reactions are exothermic according to the heats of formation calculated for the materials.³¹



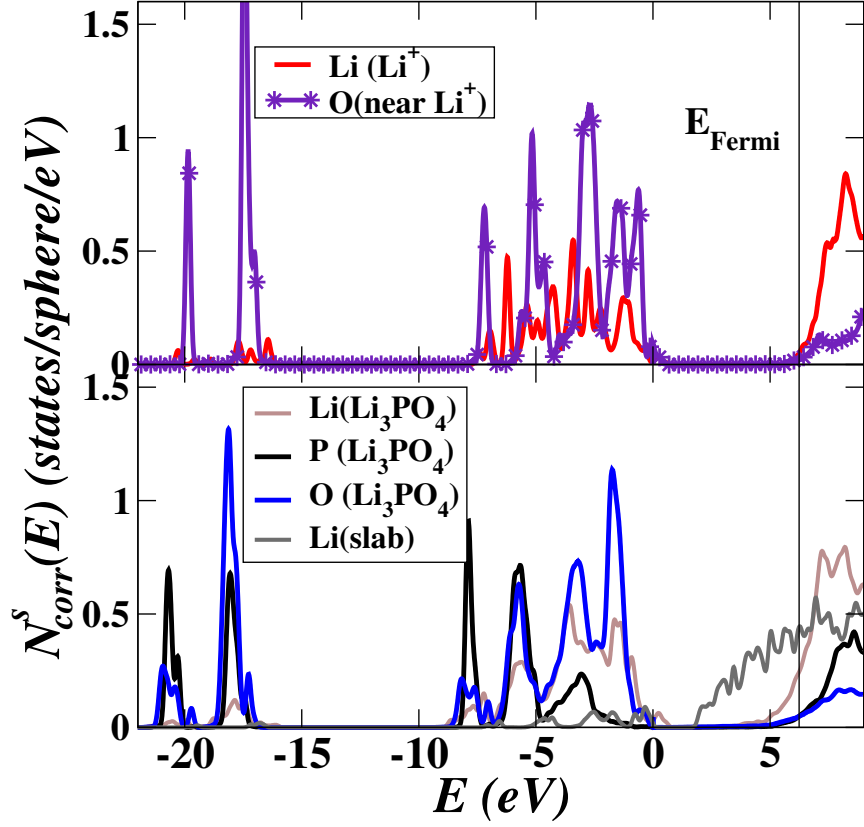


Figure 9.2: Partial density of states for β - $Li_3PO_4[010]/Li$ interface corresponding to the structure shown in Figure 9.1 calculated according equation 9.1. The contributions for the Li interstitial (Li^+) and its nearest neighbor oxygen are plotted separately. The zero of energy is set approximately at the top of the electrolyte valence band.

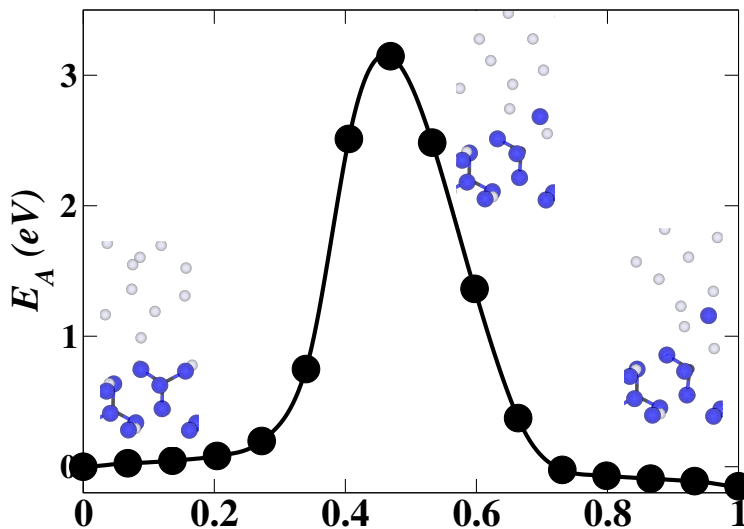


Figure 9.3: Plot of minimum energy barrier E_A (in eV) as a function of the normalized reaction coordinate for the breaking of a P-O bond at a β - $\text{Li}_3\text{PO}_4/\text{Li}$ interface as determined with the NEB approximation. The 3 inserts represent structural diagrams of the initial, maximal, and final configurations of the process using small gray, tiny black, and medium blue balls to represent Li, P, and O, respectively.

In these reactions P drastically changes its oxidation state from formally P^{+5} in Li_3PO_4 and Li_3PS_4 to P^{-3} in Li_3P . These reactions suggest that both $\text{Li}_3\text{PO}_4/\text{Li}$ and $\text{Li}_3\text{PS}_4/\text{Li}$ interfaces should be unstable at equilibrium. The result that $\text{Li}_3\text{PO}_4/\text{Li}$ interfaces are observed to be stable both computationally and experimentally⁶² suggests that there is a kinetic barrier that prevents the reaction in equation (9.2) from occurring.

I considered some aspects of this activation barrier by directly breaking a P-O bond at the interface using the nudged elastic band (NEB) method to find the minimum energy barrier between two meta-stable O positions in the system. Because the energy of breaking the P-O bond is large compared to that of rearranging the Li atoms in the Li slab, for some of my paths, including the reported one, I imposed an artificial cost for moving the Li atoms in order to stabilize the path optimization algorithm. In general, I find that moving a O from one of the PO_4 tetrahedra in Li_3PO_4 to the Li slab, often results in a net lowering of the energy of the system, as seen in Figure 9.3 and broadly consistent with equation (9.2). The NEB results for one of the many bond-breaking geometries considered are shown in Fig. 9.3 where the activation energy for the process is approximately 3 eV. This analysis is consistent with the existence of the kinetic barrier to the decomposition reaction 9.2. Apparently for the $\text{Li}_3\text{PS}_4/\text{Li}$ system no such barrier exists.

9.3 Conclusions

One of the things I observed while constructing my interface systems was that minimizing the lattice mismatch between materials did not always result in ordered interfaces. As an example, in forming an interface between the β -Li₃PO₄[010] surface and a bcc Li [100] surface, a supercell with 3 unit cells of β -Li₃PO₄ and 4 cells of bcc Li in the β -Li₃PO₄[001] direction results in a lattice mismatch of only 5%. However, the resulting configuration has more metallic Li atoms at the interface than O atoms for them to interact with. This site mismatch is highly unfavorable and attempting to optimize such an interface dramatically alters the Li structure.

For the stable interface systems studied, the interface effects are found to be confined to within a few angstroms of the interface, as shown by both the linearity of the calculated plots of $\tilde{\gamma}_{ab}(\tilde{\Omega}, n_b)$ versus n_b as well as the partial density of states analysis. This implies that these systems can be well modeled with relatively small supercells in the dimension normal to the interface. The small volume of the interface region suggests that, in the limit of perfect atomically sharp interfaces, the altered chemical environments at the interface may have a limited influence on the system.

I found a positive value for $\tilde{\gamma}_{ab}^{lim}(\tilde{\Omega})$ for all of the interfaces we considered except for Li₃PS₄/Li, which I observed to be unstable. A negative value of $\tilde{\gamma}_{ab}(\tilde{\Omega})$ implies that the bulk energies $n_a E_a + n_b E_b$ are smaller in magnitude than the total energy of the interface system $\tilde{E}_{ab}(\tilde{\Omega}, n_a, n_b)$. In other words, the interface interaction is stronger than the corresponding interactions within the bulk materials, allowing the interface to disrupt the bulk structures.

I have illustrated that interface stability is not always correctly predicted by heat of formation analysis, as shown by the stable Li₃PO₄/Li interfaces, and I explored some of the kinetic barriers that stabilize that system. For unstable systems, such as β -Li₃PS₄/Li and γ -Li₃PS₄/Li, I have shown that partial density of states analysis can be used to identify redox reactions at the interface. Specifically, I identified the occupation of conduction band states of P at the interface consistent with its expected change in oxidation state.

As noted in the recent review paper of Li and co-workers,¹² solid electrolytes have great promise for high voltage batteries in part because of their wide electrochemical windows.⁶³ In order to avoid the reduction or oxidation of the electrolyte by the electrodes and maintain the stability of the electrode/electrolyte interface, the lowest unoccupied electrolyte band must be offset above the anode Fermi level, and the highest occupied electrolyte band must be below the cathode Fermi level. This band offset model is qualitatively supported by the stability results in my simulated interfaces.

I can obtain a partial quantitative verification of our calculated offsets using my simulations of the γ -Li₃PO₄/Li system. A recent investigation by Sumita and co-workers of the LiFePO₄/ γ -Li₃PO₄ interface system based on methods similar to those employed in this work found that the Fermi level of LiFePO₄ was 1.2 eV above the top of the γ -Li₃PO₄ valence band.⁶⁴ In my simulations of the Li₃PO₄/Li interface I found that the Li Fermi level was located 4.6 eV above the γ -Li₃PO₄ valence band, similar to the gap seen in the related system shown in Figure 7.3. Using the γ -Li₃PO₄

valence band edge as a common reference, the predicted energy difference between the LiFePO_4 and Li Fermi levels is 3.4 eV, in excellent agreement with the experimentally determined value of 3.45 eV.⁹

I also demonstrated how the modeling of transport properties at electrode/electrolyte interfaces are complicated by the separation of the ionic and electronic charge. Because the internal components of a discharging battery do not maintain charge neutrality, models that do not take this into account may estimate migration barriers relevant for the open circuit battery instead.

In this work I outlined several aspects involved with the detailed modeling of solid-solid interfaces. A practical scheme was developed to compute an intensive measure of the interface interaction $\tilde{\gamma}_{ab}^{lim}(\tilde{\Omega})$, explicitly accounting for the effects of lattice strain. This scheme enables the quantitative comparison of disparate interface geometries on a consistent basis. By considering disparate interface geometries I attempted to estimate not only the most probable value of the interface energy, but the likely extent of its variation. For the cases I studied, smaller values of $\tilde{\gamma}_{ab}^{lim}$ corresponded to more physically probable interface configurations. The interface energy formalism, combined with analysis of the interface densities of states, allowed us to characterize possible interface structures and to determine their stability for several systems relevant to the further development of solid state batteries.

I identified multiple attributes that appear to be indicative of the chemical stability of the interface for these systems. The most novel of these attributes were the sign of $\tilde{\gamma}_{ab}^{lim}$ and the relative positions of the occupied and unoccupied bands for the interface materials.

For select optimized geometries I also investigated charge transfer processes across the interface, and I observed both the charge dissociation associated with a Li atom migrating into an electrolyte material and the change in oxidation states associated with reactivity at the interface.

Bibliography

- [1] D. Aurbach, Y. Gofer, Z. Lu, A. Schechter, O. Chusid, H. Gizbar, Y. Cohen, V. Ashkenazi, M. Moshkovich, R. Turgeman, and E. Levi. A short review on the comparison between Li battery systems and rechargeable magnesium battery technology. *Journal of Power Sources*, 9798:28–32, 2001.
- [2] J. Tarascon and M. Armand. Issues and challenges facing rechargeable lithium batteries. *Nature*, 414(6861):359–367, 2001.
- [3] D. P. Lide, editor. *CRC Handbook of Chemistry and Physics*. CRC PRESS, 81 edition, 2000.
- [4] M. M. Thackeray, C. Wolverton, and E. D. Isaacs. Electrical energy storage for transportation—approaching the limits of, and going beyond, lithium-ion batteries. *Energy & Environmental Science*, 5:7854–7863, 2012.
- [5] K. Mizushima, P. Jones, P. Wiseman, and J. Goodenough. Li_xCoO_2 ($0 < x < 1$): A new cathode material for batteries of high energy density. *Materials Research Bulletin*, 15(6):783–789, 1980.
- [6] A. N. Dey and B. P. Sullivan. The electrochemical decomposition of propylene carbonate on graphite. *Journal of The Electrochemical Society*, 117(2):222–224, 1970.
- [7] W. Li, J. R. Dahn, and D. S. Wainwright. Rechargeable lithium batteries with aqueous electrolytes. *Science*, 264(5162):1115–1118, 1994.
- [8] M. S. Ding, K. Xu, S. S. Zhang, K. Amine, G. L. Henriksen, and T. R. Jow. Change of conductivity with salt content, solvent composition, and temperature for electrolytes of LiPF_6 in ethylene carbonate-ethyl methyl carbonate. *Journal of The Electrochemical Society*, 148(10):A1196–A1204, 2001.
- [9] J. B. Goodenough and Y. Kim. Challenges for rechargeable Li batteries. *Chemistry of Materials*, 22(3):587–603, 2010.
- [10] M. Broussely, P. Biensan, F. Bonhomme, P. Blanchard, S. Herreyre, K. Nechev, and R. Staniewicz. Main aging mechanisms in Li ion batteries. *Journal of Power Sources*, 146(12):90–96, 2005.

- [11] A. L. Robinson and J. Janek. Solid-state batteries enter EV fray. *MRS Bulletin*, 39(12):1046–1047, 2014.
- [12] J. Li, C. Ma, M. Chi, C. Liang, and N. J. Dudney. Solid electrolyte: the key for high-voltage lithium batteries. *Advanced Energy Materials*, 5(4):1401408, 2015.
- [13] N. Kamaya, K. Homma, Y. Yamakawa, M. Hirayama, R. Kanno, M. Yonemura, T. Kamiyama, Y. Kato, S. Hama, K. Kawamoto, and A. Mitsui. A lithium superionic conductor. *Nature Materials*, 10(9):682–686, 2011.
- [14] A. Hayashi, K. Minami, F. Mizuno, and M. Tatsumisago. Formation of Li^+ superionic crystals from the $\text{Li}_2\text{S}-\text{P}_2\text{S}_5$ melt-quenched glasses. *Journal of Materials Science*, 43(6):1885–1889, 2008.
- [15] N. D. Lepley and N. A. W. Holzwarth. Computer modeling of crystalline electrolytes: Lithium thiophosphates and phosphates. *Journal of The Electrochemical Society*, 159(5):A538–A547, 2012.
- [16] W. Kohn and L. J. Sham. Self-consistent equations including exchange and correlation effects. *Physical Review*, 140:A1133–A1138, 1965.
- [17] J. P. Perdew and Y. Wang. Accurate and simple analytic representation of the electron-gas correlation energy. *Physical Review B*, 45:13244–13249, 1992.
- [18] J. P. Perdew, K. Burke, and M. Ernzerhof. Generalized gradient approximation made simple. *Physical Review Letters*, 77:3865–3868, 1996.
- [19] A. Sutton and R. Balluffi. *Interfaces in Crystalline Materials*. Oxford Classic Texts in the Physical Sciences. Clarendon Press, 1995.
- [20] R. Benedek, D. N. Seidman, and C. Woodward. The effect of misfit on heterophase interface energies. *Journal of Physics: Condensed Matter*, 14(11):2877, 2002.
- [21] M. W. Finnis. The theory of metal-ceramic interfaces. *Journal of Physics: Condensed Matter*, 8(32):5811, 1996.
- [22] J. Hartford. Interface energy and electron structure for Fe/VN. *Phys. Rev. B*, 61:2221–2229, 2000.
- [23] A. Hashibon, C. Elsasser, and M. Ruhle. Structure at abrupt copper-alumina interfaces: An ab initio study. *Acta Materialia*, 53(20):5323–5332, 2005.
- [24] M. Benoit, C. Langlois, N. Combe, H. Tang, and M.-J. Casanove. Structural and electronic properties of the Au(001)/Fe(001) interface from density functional theory calculations. *Physical Review B*, 86(7), 2012.
- [25] S. Lu, Q.-M. Hu, M. P. J. Punkkinen, B. Johansson, and L. Vitos. First-principles study of fcc-Ag/bcc-Fe interfaces. *Physical Review B*, 87(22), 2013.

- [26] E. Fu, Y. Fang, M. Zhuo, S. Zheng, Z. Bi, Y. Wang, M. Tang, X. Ding, W. Han, H. Luo, J. Baldwin, A. Misra, and M. Nastasi. Interface structure of Nb films on single crystal MgO(100) and MgO(111) substrates. *Acta Materialia*, 64:100–112, 2014.
- [27] P. Hohenberg and W. Kohn. Inhomogeneous electron gas. *Physical Review*, 136:B864–B871, 1964.
- [28] P. Giannozzi, S. Baroni, N. Bonini, M. Calandra, R. Car, C. Cavazzoni, D. Ceresoli, G. L. Chiarotti, M. Cococcioni, I. Dabo, A. D. Corso, S. de Gironcoli, S. Fabris, G. Fratesi, R. Gebauer, U. Gerstmann, C. Gougoussis, A. Kokalj, M. Lazzeri, L. Martin-Samos, N. Marzari, F. Mauri, R. Mazzarello, S. Paolini, A. Pasquarello, L. Paulatto, C. Sbraccia, S. Scandolo, G. Sclauzero, A. P. Seitsonen, A. Smogunov, P. Umari, and R. M. Wentzcovitch. Quantum espresso: a modular and open-source software project for quantum simulations of materials. *Journal of Physics: Condensed Matter*, 21(39):394402 (19pp), 2009.
- [29] P. E. Blöchl. Projector augmented-wave method. *Physical Review B*, 50:17953–17979, 1994.
- [30] N. A. W. Holzwarth, A. R. Tackett, and G. E. Matthews. A Projector Augmented Wave (PAW) code for electronic structure calculations, Part I: *atompaw* for generating atom-centered functions. *Computer Physics Communications*, 135:329–347, 2001.
- [31] N. D. Lepley, N. A. W. Holzwarth, and Y. A. Du. Structures, Li⁺ mobilities, and interfacial properties of solid electrolytes Li₃PS₄ and Li₃PO₄ from first principles. *Physical Review B*, 88:104103, 2013.
- [32] N. A. W. Holzwarth, G. E. Matthews, R. B. Dunning, A. R. Tackett, and Y. Zeng. Comparison of the projector augmented wave, pseudopotential, and linearized augmented plane wave formalisms for density functional calculations of solids. *Physical Review B*, 55:2005–2017, 1997.
- [33] H. Jónsson, G. Mills, and K. W. Jacobsen. Nudged elastic band method for finding minimum energy paths of transitions. In B. J. Berne, G. Ciccotti, and D. F. Coker, editors, *Classical and Quantum Dynamics in Condensed Phase Simulations*, pages 385–404. World Scientific, Singapore, 1998.
- [34] G. Henkelman, B. P. Uberuaga, and H. Jónsson. A climbing image nudged elastic band method for finding saddle points and minimum energy paths. *Journal Chemical Physics*, 113:9901–9904, 2000.
- [35] G. Henkelman and H. Jónsson. Improved tangent estimate in the nudged elastic band method for finding minimum energy paths and saddle points. *Journal Chemical Physics*, 113:9978–9985, 2000.

- [36] L. Bengtsson. Dipole correction for surface supercell calculations. *Physical Review B*, 59:12301–12304, 1999.
- [37] A. Kokalj. XCrySDen— an new program for displaying crystalline structures and densities. *Journal of Molecular Graphics and Modelling*, 17:176–179, 1999.
- [38] A. Kokalj. Computer graphics and graphical user interfaces as tools in simulations of matter at the atomic scale. *Computational Materials Science*, 28:155–168, 2003.
- [39] K. Momma and F. Izumi. Vesta 3 for three-dimensional visualization of crystal, volumetric, and morphology data. *Applied Crystallography*, 44:1272–1276, 2011.
- [40] D. A. Young. *Phase Diagrams of the Elements*. University of California Press, 1991. ISBN 0-520-07483-1.
- [41] M. Hanfland, K. Syassen, N. Christensen, and D. Novikov. New high-pressure phases of lithium. *Nature*, 408(6809):174–178, 2000.
- [42] E. A. Mikajlo, K. L. Nixon, V. A. Coleman, and M. J. Ford. The electronic band structure of Li_2O : Testing theoretical predictions using electron momentum spectroscopy. *Journal of Physics: Condensed Matter*, 14(13):3587, 2002.
- [43] M. Hayoun and M. Meyer. Surface effects on atomic diffusion in a superionic conductor: A molecular dynamics study of lithium oxide. *Surface Science*, 607(0):118–123, 2013.
- [44] M. M. Islam and T. Bredow. Density functional theory study for the stability and ionic conductivity of Li_2O surfaces. *The Journal of Physical Chemistry C*, 113(2):672–676, 2009.
- [45] A. Lichanot, M. Gelize, C. Larrieu, and C. Pisani. Hartree-fock ab initio study of relaxation and electronic structure of lithium oxide slabs. *Journal of Physics and Chemistry of Solids*, 52(9):1155–1164, 1991.
- [46] W. Mackrodt. Atomistic simulation of oxide surfaces. *Physics and chemistry of minerals*, 15(3):228–237, 1988.
- [47] T. Ouazzani, A. Lichanot, and C. Pisani. Effect of the quality of the atomic orbitals basis set on the relaxation and electronic structure of the (110) surface of lithium oxide. *Journal of Physics and Chemistry of Solids*, 56(7):915 – 918, 1995.
- [48] M. D. Radin, J. F. Rodriguez, F. Tian, and D. J. Siegel. Lithium peroxide surfaces are metallic, while lithium oxide surfaces are not. *Journal of the American Chemical Society*, 134(2):1093–1103, 2012.
- [49] N. Seriani. Ab initio thermodynamics of lithium oxides: from bulk phases to nanoparticles. *Nanotechnology*, 20(44):445703, 2009.

- [50] A. Sutjianto, S. Tam, R. Pandey, L. Curtiss, and C. Johnson. Ab initio calculations for dissociative hydrogen adsorption on lithium oxide surfaces. *Journal of Nuclear Materials*, 219(0):250–258, 1995.
- [51] M. Nagao, A. Hayashi, and M. Tatsumisago. High-capacity Li_2S -nanocarbon composite electrode for all-solid-state rechargeable lithium batteries. *J. Mater. Chem.*, 22:10015–10020, 2012.
- [52] M. Eom, J. Kim, S. Noh, and D. Shin. Crystallization kinetics of $\text{Li}_2\text{SP}_2\text{S}_5$ solid electrolyte and its effect on electrochemical performance. *Journal of Power Sources*, 284(0):44–48, 2015.
- [53] J.-G. Li. Wetting and interfacial bonding of metals with ionocovalent oxides. *Journal of the American Ceramic Society*, 75(11):3118–3126, 1992.
- [54] N. Kamaya, K. Homma, Y. Yamakawa, M. Hirayama, R. Kanno, M. Yonemura, T. Kamiyama, Y. Kato, S. Hama, K. Kawamoto, and A. Mitsui. A lithium superionic conductor. *Nature Materials*, 10(9):682–686, 2011.
- [55] Z. Liu, W. Fu, E. A. Payzant, X. Yu, Z. Wu, N. J. Dudney, J. Kiggans, K. Hong, A. J. Rondinone, and C. Liang. Anomalous high ionic conductivity of nanoporous $\beta\text{-Li}_3\text{PS}_4$. *Journal of the American Chemical Society*, 135(3):975–978, 2013.
- [56] T. Yamada, S. Ito, R. Omoda, T. Watanabe, Y. Aihara, M. Agostini, U. Ulissi, J. Hassoun, and B. Scrosati. All solid-state lithium–sulfur battery using a glass-type $\text{P}_2\text{S}_5\text{-Li}_2\text{S}$ electrolyte: Benefits on anode kinetics. *Journal of The Electrochemical Society*, 162(4):A646–A651, 2015.
- [57] Y.-X. Chen and P. Kaghazchi. Metalization of Li_2S particle surfaces in Li-S batteries. *Nanoscale*, 6(22):13391–13395, 2014.
- [58] H. Park, H. S. Koh, and D. J. Siegel. First-principles study of redox end members in lithium-sulfur batteries. *The Journal of Physical Chemistry C*, 119(9):4675–4683, 2015.
- [59] K. C. Santosh, R. C. Longo, K. Xiong, and K. Cho. Electrode-electrolyte interface for solid state Li-ion batteries: Point defects and mechanical strain. *Journal of The Electrochemical Society*, 161(11):F3104–F3110, 2014.
- [60] L. Bengtsson. Dipole correction for supercell calculations. *Physical Review B*, 59:12301–12304, 1999.
- [61] K. C. Santosh, K. Xiong, R. C. Longo, and K. Cho. Interface phenomena between Li anode and lithium phosphate electrolyte for Li-ion battery. *Journal of Power Sources*, 244:136–142, 2013.
- [62] D. Danilov, R. A. H. Niessen, and P. H. L. Notten. Modeling all-solid-state Li-ion batteries. *Journal of The Electrochemical Society*, 158(3):A215, 2011.

- [63] J. B. Goodenough and K.-S. Park. The Li-Ion Rechargeable Battery: A Perspective. *Journal of the American Chemical Society*, 135(4):1167–1176, 2013.
- [64] M. Sumita, Y. Tanaka, M. Ikeda, and T. Ohno. Theoretically designed $\text{Li}_3\text{PO}_4(100)/\text{LiFePO}_4(010)$ coherent electrolyte/cathode interface for all solid-state Li ion secondary batteries. *The Journal of Physical Chemistry C*, 119(1):14–22, 2015.

Part III
Curriculum Vitae

Nicholas D. Lepley

EDUCATION

Graduate:

Wake Forest University 2013-2015

PhD, Physics

- Dissertation title: First principles investigations of solid-solid interfaces in lithium battery materials

Wake Forest University 2009-2013

MS, Physics

- Thesis title: An investigation of lithium solid electrolyte materials with first principles calculations

Wake Forest University 2009-2012

Computer Science

- Coursework on theory of computation, data structures, numerical methods, optimization, and high-performance computing

Undergraduate:

Wake Forest University 2006-2009

BS/BA, Physics/English

- Graduated in 3 years
- Division I athlete (Atlantic Coast Conference)

PUBLICATIONS

- [6] **N. D. Lepley** and N. A. W. Holzwarth. Modeling interfaces between solids: Application to Li battery materials. *Physical Review B*, Under review.
- [5] **N. D. Lepley**, N. A. W. Holzwarth, and Y. Du. Structures, Li^+ mobilities, and interfacial properties of solid electrolytes Li_3PS_4 and Li_3PO_4 from first principles. *Physical Review B*, 88:104103, 2013.
- [4] **N. D. Lepley** and N. A. W. Holzwarth. Computer modeling of crystalline electrolytes: Lithium thiophosphates and phosphates. *Journal of The Electrochemical Society*, 159(5):A538–A547, 2012.
- [3] N. A. W. Holzwarth, **N. D. Lepley**, and Y. Du. Computer modeling of lithium phosphate and thiophosphate electrolyte materials. *Journal of Power Sources*, 196(16):6870–6876, 2011.
- [2] **N. D. Lepley** and N. A. W. Holzwarth. Computer modeling of crystalline electrolytes- lithium thiophosphates and phosphates. *ECS Transactions*, 35(14):39–51, 2011.
- [1] M. Torrent, N. A. W. Holzwarth, F. Jollet, D. Harris, **N. D. Lepley**, and X. Xu. Electronic structure packages: Two implementations of the projector augmented wave (PAW) formalism. *Computer Physics Communications*, 181(11):1862–1867, 2010.

EXPERIENCE

Wake Forest University Physics Department 2009-2015

Graduate Researcher: Computational materials design (Thesis work)

- Evaluated published literature
- Designed and carried out relevant investigations
- Performed and analyzed simulations using large scientific codes
- Wrote peer-reviewed publications and presented results at national and international meetings

Quantlab Financial 2013

Research Intern

- Used technical analysis to develop nonlinear models for asset prices

Kaplan Test Prep 2009-2010
Instructor

- Classroom instructor covering materials and techniques for national standardized tests
- Rated "Good or Excellent" by 100% of students

Wake Forest Nanotechnology Center 2008-2009
Researcher: Applied thermoelectrics

- Designed, constructed, and programmed experimental apparatus to measure the thermoelectric properties of carbon nanotube/polymer composites.

Wake Forest Computer Science Department 2008
Researcher: Multispectral data analysis

- Performed factor analysis on large, multispectral data sets to improve burn diagnostics

AWARDS

- Wake Forest 3 Minute Thesis competition (1st, judges vote) 2015
 - *Talk*: The many-body problem and practical quantum mechanics
- Wake Forest 3 Minute Thesis competition (1st, audience vote) 2015
- Wake Forest 3 Minute Thesis competition (1st) 2014
 - *Talk*: Computational design of novel Li batteries
- Wake Forest Physics Graduate Scholarship 2009-2015
- Chambers Entrepreneurship Grant 2012
- Wake Forest Research Fellowship 2008

SKILLS

General:

- Research
- Physics
- Public speaking
- Writing (scientific, technical, creative)
- Teaching
- Mathematical modeling
- L^AT_EX and MS Office

Computational:

- Perl (use daily)
- Python (occasional)
- C/C++ (coursework)
- FORTRAN (occasional)
- Scripting (perl, python, bash/zsh)
- Standard mathematics computational packages (e.g. Maple, MATLAB/Octave, Mathematica, gnuplot)

POSTERS AND PRESENTATIONS

- Investigating Li-ion solid electrolytes using simulations based on density functional theory
 - Winston-Salem, NC. Wake Forest Physics Colloquium Series (2015). *Invited talk*
- Modeling Solid-Electrolyte/Electrode Interfaces
 - San Antonio, TX. APS March Meeting (2015).
- Modeling Solid-Electrolyte/Electrode Interfaces
 - Madison, WI. Transformational Technologies in Molecular Simulations Workshop (2014).
- Surface Structure and Stability in Li₃PS₄ and Li₃PO₄ Electrolytes from First Principles.
 - Baltimore, MD. APS March Meeting (2013).
- Computer Modeling of Crystalline Electrolytes - Lithium Thiophosphates and Phosphates.
 - Winston-Salem, NC. Electronic Structure Workshop (2012).
- First principles investigation of the superionic electrolyte Li₇P₃S₁₁.
 - Boston, MA. APS March Meeting (2012).
- Computer Modeling of Crystalline Electrolytes - Lithium Thiophosphates and Phosphates.
 - Dallas, TX. APS March Meeting (2011).
- Computer Modeling of Lithium Phosphate and Thiophosphate Electrolyte Materials
 - Montreal, Canada. International Meeting on Li-ion Batteries (2010).
- Hyperspectral data mining for burn diagnostics.
 - Winston-Salem, NC. Wake Forest Undergraduate Research Day (2008).